IEEE Access
Multidisciplinary ⋮ Rapid Review ⋮ Open Access Journal

Received 2 March 2024, accepted 8 March 2024, date of publication 18 March 2024, date of current version 2 April 2024.

Digital Object Identifier 10.1109/ACCESS.2024.3376468

RESEARCH ARTICLE

A Hybrid Sparrow Search Optimized Fractional Virtual Inertia Control for Frequency Regulation of Multi-Microgrid System

BASHAR ABBAS FADHEEL[1,2], NOOR IZZRI ABDUL WAHAB[1], (Senior Member, IEEE), PREMKUMAR MANOHARAN[3,4], (Senior Member, IEEE), ALI JAFER MAHDI[5,6], MOHD AMRAN BIN MOHD RADZI[1], (Senior Member, IEEE), AZURA BINTI CHE SOH[1], (Senior Member, IEEE), HUSSEIN MOHAMMED RIDHA[1,7], ANAS R. ALSOUD[8], VEERAPANDIYAN VEERASAMY[9], (Member, IEEE), ANDREW XAVIER RAJ IRUDAYARAJ[1], (Graduate Student Member, IEEE), AND BIZUWORK DEREBEW ALEMU[10]

[1]Advanced Lightning, Power, and Energy Research (ALPER), Department of Electrical and Electronics Engineering, Faculty of Engineering, Universiti Putra Malaysia (UPM), Serdang 43400, Malaysia
[2]Department of Biomedical Engineering, University of Kerbala, Karbala 56001, Iraq
[3]Department of Electrical and Electronics Engineering, Dayananda Sagar College of Engineering, Bengaluru, Karnataka 560078, India
[4]Department of Electrical and Electronics Engineering, College of Engineering, Institute of Power Engineering (IPE), Universiti Tenaga Nasional (UNITEN), Kajang, Putrajaya, Selangor 43000, Malaysia
[5]College of Information Technology Engineering, Al-Zahraa University for Women, Karbala 56001, Iraq
[6]Department of Electrical and Electronics Engineering, University of Kerbala, Karbala 56001, Iraq
[7]Department of Computer Engineering, Mustansiriyah University, Baghdad 14022, Iraq
[8]Hourani Center for Applied Scientific Research, Al-Ahliyya Amman University, Amman 19328, Jordan
[9]School of Electrical and Electronic Engineering, Nanyang Technological University, Singapore 639798
[10]Department of Statistics, College of Natural and Computational Science, Mizan-Tepi University, Teppi, Ethiopia

Corresponding authors: Premkumar Manoharan (mprem.me@gmail.com) and Bizuwork Derebew Alemu (bizuworkd@mtu.edu.et)

ABSTRACT This paper introduces a robust approach, integrating a Virtual Inertia Controller (VIC) with a modified demand response controller for an islanded Multi-Microgrid (MMG) system, accommodating high levels of Renewable Energy Sources (RESs). In these MGs, the low inertia in the system has an undesirable impact on the stability of MG frequency. As a result, it leads to a weakening of the MGs overall performance. A novel fractional derivative virtual inertia is integrated into the VIC loop to address this issue. This enhancement aims to fortify the MG's stability and robust performance, particularly when facing contingencies. Furthermore, a modified demand response controller has been incorporated into the proposed inertia control technique to mitigate the frequency fluctuations and reduce stress on the energy storage system (ESS). Fractional Order Proportional Integral Derivative (FOPID) controllers have been employed to regulate the active power output of the biodiesel generators and the Geothermal station in the MG. The hybrid sparrow search and mountain gazelle optimizer algorithm (SSAMGO) optimizes the parameters for the three-loop controller. Time-domain simulations assess the effectiveness of proposed controllers in enhancing system frequency stability. SSAMGO's performance was comprehensively evaluated, comparing it to various optimization algorithms in diverse scenarios. The results obtained from the MMG system demonstrate that utilizing the proposed controller technique, optimized with hybrid SSAMGO parameters, yields notable improvements in settling time by 24.68%, 46.20%, 7.52%, and 61.01%, steady-state error values by 72.56%, 98.18%, 98.73%, and 6.67%, undershoot by 105.76%, 144.23%, 19.23%, and 7.69% compared to other state-of-the-art algorithms presented in the literature. Finally, the proposed control technique's effectiveness and robustness are assessed in comparison to conventional inertia control across various system scenarios. These scenarios encompass random load demand fluctuations, real-time changes in RES, and a wide spectrum of system operations, including situations with reduced damping and inertia and high levels of load variation.

The associate editor coordinating the review of this manuscript and approving it for publication was Sotirios Goudos.

© 2024 The Authors. This work is licensed under a Creative Commons Attribution-NonCommercial-NoDerivatives 4.0 License.
For more information, see https://creativecommons.org/licenses/by-nc-nd/4.0/

INDEX TERMS Virtual inertia control, load frequency control, renewable energy resources, hybrid optimization algorithm, demand response control, power system stability, microgrid system.

I. INTRODUCTION

The intermittent nature of Renewable energy sources (RESs) in Microgrids (MGs) makes it challenging to stabilize the system frequency within acceptable limits. The over-penetration of RESs can result in precarious frequency oscillations, exacerbating the difficulty of maintaining system stability [1]. Moreover, the integration of RESs into islanded MGs leads to a reduction in the overall system inertia [2]. Hence, this study introduces an enhanced model of an MMG electric power system that incorporates a high penetration of RESs. The focus is on frequency analysis and control, where new virtual inertia control techniques are proposed. Additionally, the effects of demand response are taken into consideration in the analysis.

To overcome the challenge of lacking inertia in MGs, the VIC technique is one of the significant solutions that has been used widely. In [3], the authors proposed a derivative VIC connected with a superconducting ESS to compensate required inertia of the system. Reference [4] introduces the derivatives virtual inertia technique to improve the frequency dynamic response of interconnected power systems with RESs. However, it neglects the effect of damping the control loop in the structure of the controllers. The ability to provide the effect of virtual damping has been considered in [5], which significantly affects the transient and steady-state stability of the performance of the system frequency. In [6], a VIC technique to support a single-area MG system with the required inertia from a photovoltaic system is presented. The model includes virtual damping and a droop control loop in [7] to enhance stability. In [8], the author proposed a fractional order VIC approach to address frequency fluctuations in islanded MG power systems. Previous studies have employed derivative control techniques with integer derivative orders. However, this approach results in a higher virtual inertia constant value for the VIC system. Therefore, a larger ESS capacity is required to compensate for active power fluctuations during disturbances effectively.

Furthermore, in recent years, there has been a significant focus on demand response controller (DRC) techniques for frequency control. These techniques have gained considerable attention due to their potential in addressing the challenges associated with maintaining grid frequency stability. In [9], the author introduces a DR control technique aimed at improving the frequency performance of interconnected hybrid power systems. The authors in [10] demonstrated that incorporating an ESS into the system significantly improved the dynamic stability by actively participating in DR measures. In [11], the authors propose a method that combines a particle swarm optimization algorithm (PSO) with a DR controller technique to improve the system stability through the optimization of ESS's size. The authors of [12] propose an approach that integrates the ESS control loop with the LFC system. By doing so, they aim to enhance the overall system stability and mitigate frequency deviations. To achieve this, the PSO algorithm is utilized to determine the optimal parameters for the Fuzzy controller within the secondary control loop.

Over the years, researchers have proposed numerous classical and intelligence-based control strategies with the primary goal of enhancing system stability, reducing frequency deviation, and minimizing the tie-line power flow variation. These strategies have been specifically designed to tackle the complex challenges inherent in MG power systems, with the ultimate aim of ensuring seamless operation and optimizing performance [13]. In [14], the PID controller parameters were tuned using the Ziegler-Nichols (Z-N) method, yielding effective results under certain conditions. However, when dealing with a system that exhibits substantial uncertainties in its load and generation dynamics, this approach becomes inadequate. As a consequence, alternative control strategies need to be investigated to address and overcome the complexities introduced by these uncertainties. To address these challenges, researchers in [15] utilized type-2 fuzzy tuning for PID controller parameters. Stability was ensured through a Lyapunov function, and tuning laws for output scaling factors and consequent parameters were derived, resulting in improved system performance. In [16] and [17], the author proposes a fuzzy-PSO-PID controller designed to regulate frequency deviations in a Hydro-Hydro Power System. It assesses the controller's effectiveness in handling load alterations and compares its performance with existing LFC approaches. The research targets the optimization of LFC in hydro systems to enhance power delivery efficiency, considering the varying demands and mechanical constraints of hydro turbines. The self-adaptive nature of Neural Network-based classical controllers allows them to handle uncertainty in dynamic systems. However, the effectiveness of these controllers is contingent upon a properly designed network; otherwise, their performance may degrade [18]. Researchers employ population-based evolutionary computational intelligence approaches such as PSO [19], Fuzzy inference system [20], Manta Ray Foraging [21], and numerous other methods. The controller gain values obtained from the above classical method have improved MG system efficiency and robustness. However, with the rapid growth of MMG systems and the unpredictable variations in RESs and load demand, there is a pressing need for an even more efficient controller to manage these uncertainties effectively. Conventional approaches struggle and degrade in performance with exponential uncertainty growth and lacking MG inertia impact. Maintaining stability in MG power systems remains a significant challenge due to the lack of optimal control parameter settings. To address this, researchers have introduced an alternative control concept

of FOPID to enhance the performance of classical integer order controllers and increase robustness in the face of uncertainties.

The additional tuning parameters of differential-integral operators introduce a high degree of freedom [22]. These additional features contribute to its distinctive performance in various applications [23]. In conjunction with intelligence-based heuristic methods, the FOPID controller has demonstrated significant effectiveness in diverse LFC applications for MG power systems, such as using Quasi-Oppositional Sine Cosine Algorithm (QOSCA) tuned FOPID gain parameters in [24], Jellyfish Search Optimizer (JSO) in [25], and Cohort Intelligence Optimizer (CIO) in [26]. However, the literature mentioned above overlooks the investigation of high penetration RESs like wind turbine power, solar thermal power, geothermal stations, solar PV, and ESSs, considering the significant reduction in the equivalent inertia constant in MMG power systems. This research gap serves as a driving force for researchers to explore the influence of these factors on LFC systems when utilizing the FOPID controller.

On the other hand, designing PID/FOPID controller gain values using optimization techniques typically entails choosing one or more performance indices for the controller. These indices may include Integral Absolute Error (IAE), Integral Time Absolute Error (ITAE), Integral Square Error (ISE), and Integral Time Absolute Error (ITSE) [27]. In optimization-based design methods, ISE is often preferred for its mathematical convenience, particularly in scenarios with step changes in set-point or load. Its computational differentiability enables the use of gradient-based optimization techniques for obtaining FOPID controller gains. Nevertheless, ISE tends to mitigate significant errors in the system, leading to higher controller gain values, oscillatory step responses, and a potential loss of robustness [28]. To address this, employing IAE or ITSE as performance indices emphasizes small errors in controller gain tuning over ISE. Conversely, ITAE prioritizes minimizing error during the initial transient response and penalizes prolonged larger errors through the integration of absolute error multiplied by time. Systems optimized with ITAE generally achieve faster settling times than alternatives, potentially with a slower initial response [23].

The dynamic performance of the proposed model is enhanced through the implementation of three stages of controller techniques in this paper. To enhance the frequency response and minimize the variations in tie line power during load disturbances in a low-inertia MG system integrated with RESs, a new fractional derivative virtual inertia control technique named (FDVIC) is devised. To further enhance the frequency response within the primary control loop and reduce the strain on the ESS during charging and discharging, a combined approach is adopted by integrating the demand response controller (DRC) with the proposed FDVIC. This integration aims to improve system performance synergistically. In the last stage, the secondary control loop involves the utilization of FOPID controllers to govern the output active power of the biodiesel generators and the geothermal generator. The contribution of this study can be summarized as below:

1) To mitigate the frequency nadir of the MG system during load disturbances, a novel FDVIC is developed. The objective is to reduce the lowest frequency point experienced by the system.
2) To enhance the primary control loop and alleviate stress on the ESS of the FDVIC, the DR controller is integrated with the FDVIC. This integration aims to improve the overall performance of the system stability by leveraging the capabilities of both controllers.
3) To improve the performance of the SSA algorithm, a hybridization approach with the MGO algorithm is employed. This hybridized algorithm is then applied to tune the parameters of the FDVIC, DRC, and FOPID controllers in the virtual control loop, primary control loop, and secondary control loop, respectively, within the MG system.
4) To assess the efficiency of the SSAMGO-tuned FOPID controller, a comprehensive comparison is conducted using steady-state and transient performance indices. The results clearly indicate that the SSAMGO-tuned FOPID controller outperforms other state-of-the-art techniques.

The rest of this paper is structured as follows: Section II details the proposed MG model. Section III provides a demonstration of the proposed control strategy. Section IV introduces the hybrid optimization algorithm. Section V presents the simulation results and corresponding discussion. Finally, Section VI summarizes the conclusions derived from this study.

II. MULTI-MG MODEL DESCRIPTION

The development and economic growth of Malaysia have led to an increased demand for energy within the country. In response to this demand, Malaysia has emerged as a promising nation in the utilization of various RESs. These resources include biodiesel, wind energy, solar energy, and geothermal energy [29]. In the present study, the MMG power system consists of an MG1 with a rated capacity of 2000 kW and an MG2 with a capacity of 1500 kW. MG1 consists of a biodiesel generator with a 600 kW rated power integrated with a 350 kW rated wind turbine generator (WTG), a 550 kW solar thermal generator (STH), and a 550 kW geothermal power station. MG2 consists of a 550 kW-rated WTG, a 400 kW-capacity solar photovoltaic, and a 600 kW-rated biodiesel generator. In addition, MG1 can deliver power to a residential load of 800 kW, and MG2 is capable of supplying a residential load of 600 kW. For demand response control, 30% of the total nominal load of MG1, totaling 240 kW, has been chosen as responsive loads. Similarly, MG2 has designated 25% of its total nominal load, amounting to 187.5 kW, for demand response control. A 300 kW ESS has been combined with MG1 and MG2 to provide the MG

system with the required inertia utilizing the novel FDVIC technique that has been proposed. The MMG development structure proposed in this paper is illustrated in Fig. 1.

The frequency stability is an effect of the MG's inertia response. During load imbalance or load fluctuation events, inertia plays an important role in maintaining the frequency of the MG system [30]. The inertia control stage is the first line of defence against load fluctuations to reduce the frequency deviation of the MG. The inertia constant of the conventional system is calculated as a function of the kinetic energy stored in the generator's rotating parts.

The inertia can be calculated as follows:

$$H = \frac{E_{kinetic}}{S} = \frac{J\omega^2}{2S} \tag{1}$$

where H is the inertia constant; $E_{kinetic}$ is the stored kinetic energy in the rotor; J is the moment of inertia in kgm^2; ω is the rotor angular velocity in rad/s, and S is the rated power of the MG system in VA.

The equivalent inertia of the MMG system integrated with RESs can be estimated as follows:

$$H_{equiv.} = \frac{\sum_{i=1}^{N} H_i S_i}{\sum_{i=1}^{N} S_i + \sum_{i=1}^{R} P_i} \tag{2}$$

$$D_{equiv.} = \frac{\sum_{i=1}^{N} D_i S_i}{\sum_{i=1}^{N} S_i + \sum_{i=1}^{R} P_i} \tag{3}$$

where H_i is the inertia constant of the ith MG distributed generators (i = 1, 2, ... N); N is the number of distributed generators; S_i is the rating power of the ith MG distributed generators; D_i is the damping coefficient of the ith MG distributed generators; P_i is the injected real power by the ith RESs connected to MG by static converters (zero inertia); R is number of RESs.

The dynamic response of the generation-load power imbalance is described by the following general swing equation [6]:

$$\Delta P_m - \Delta P_{load} = 2H\frac{d\Delta f}{dt} + D\Delta f \tag{4}$$

where ΔP_m is the change of mechanical power, ΔP_{load} is the change of demand load, and Δf is the rate of change of the MG frequency.

Fig. 2 shows that the proposed dynamic model consists of the secondary control loop with FOPID, the proposed FDVIC, and DRC. The parameters of the proposed MGs and RESs are illustrated in Appendix A.

A. BIODIESEL GENERATOR

Biodiesel Generator (BDG) is made by a chemical process called transesterification, and it has similar qualities to natural diesel despite being made from energy crops that are inexpensive in cost and maintenance [31]. It can be utilized in various combinations, including its pure form (B100). The linearized model of the BDG output power can be approximated as follows [9]:

$$\Delta P_{BDG} = \frac{k_{VA}}{1 + sT_{VA}} \cdot \frac{k_{BE}}{1 + sT_{BE}} \tag{5}$$

where ΔP_{BDG} is the output power of the BDG; k_{VA}, T_{VA}, k_{BE}, and T_{BE} are valve gain, valve actuator delay, engine gain, and time constants of BDG, respectively.

B. GEOTHERMAL POWER STATION

Geothermal power stations (GEO), which use the heat stored deep inside the earth to produce electricity, are another promising form of renewable energy. The high-pressure (>7 bar), high-temperature (140 to 250 degrees Celsius) stream is injected straight into the GEO power plant. According to the International GEO Association (IGA), the capacity that has been installed around the world is around 12.636 GW, and it has produced 73.549 GWh of electrical energy. The linearized transfer function model of geothermal energy conversion is considered in this study as follows [32]:

$$\Delta P_{Geo} = \frac{k_{gg}}{1 + sT_{gg}} \cdot \frac{k_{tg}}{1 + sT_{tg}} \tag{6}$$

where ΔP_{Geo} is the output power of the GEO; k_{gg}, T_{gg}, k_{tg}, and T_{tg} are governor gain, governor time constant, turbine gain, and turbine time constant, respectively.

C. SOLAR THERMAL GENERATOR

Malaysia's daily solar radiation, averaging 4000–5000 Wh/m^2 and 4–8 hours of daily sunshine, highlights its strong solar energy potential. These favourable conditions position the country for widespread adoption of solar technologies, including solar water heaters in diverse economic sectors [33]. Solar Thermal (STH) power plant consists of trough collectors, several dishes to reflect the sun's heat, a central receiver, and a linear fresnel reflector. The generated steam powers a turbine coupled to an alternator for electricity production. Excess heat from the working fluid is stored in molten salt for post-sunset utilization [34]. The transfer function of the STH system is depicted in (7):

$$\Delta P_{STH} = \frac{k_T}{1 + sT_T} \cdot \frac{k_S}{1 + sT_S} \tag{7}$$

where ΔP_{STH} is the output power of the STH power plant; k_T, T_T, k_s, and T_s are the gain of the system turbine, the turbine charging time constant, the solar collector gain, and the time constant of the solar collector, respectively.

D. WIND TURBINE GENERATOR

Recent technological progress in power converters, reduced reliance on fossil fuels, environmental considerations, and cost-effectiveness have elevated wind power as a critical renewable energy source [35]. A pitch control mechanism changes the rotor's pitch as the wind speed changes in order

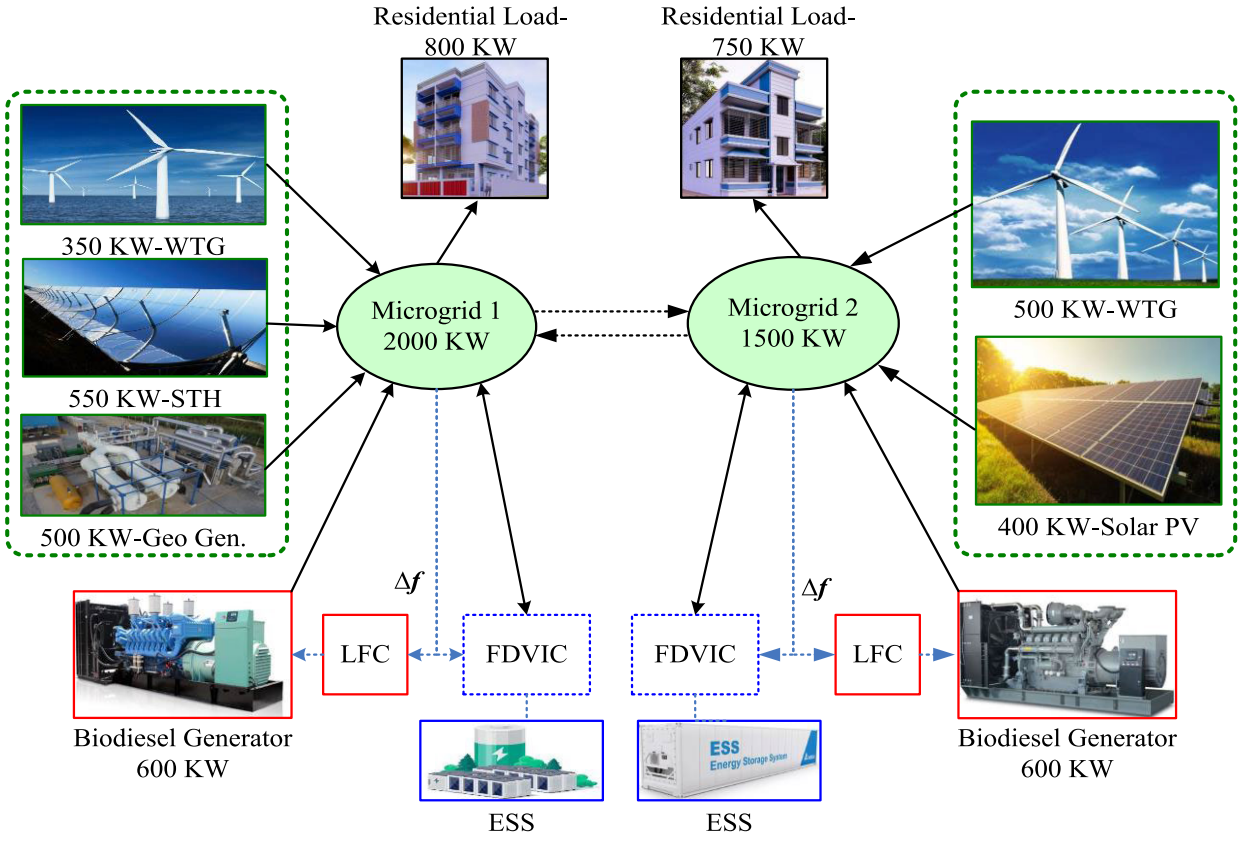

FIGURE 1. Block diagram of the MMG model.

to maintain the steady output of power from the wind energy conversion system. Wind-generated power relies on various factors. The mechanical power of wind turbines is determined by [36]:

$$\Delta P_{WT} = \frac{1}{2}\rho A_r C_p V_W^3 \tag{8}$$

$$C_p = (0.44 - 0.0167\beta)\sin\left[\frac{\pi(\lambda - 3)}{15 - 0.3\beta}\right] - 0.018(\lambda - 3)\beta \tag{9}$$

where ΔP_{WT} represents the mechanical power extracted from the wind; ρ is the air density in Kg/m^3; A_r is the swept area of the blades (m^2); V_W is the wind speed, and C_p is a function influenced by both the speed tip ratio (λ) and blade pitch angle (β). The association between mechanical power and β allows for the utilization of this relationship to reserve power. Two WTGs integrated with MG1 and MG2 are considered in this study and illustrated as a first-order transfer function as follows:

$$\Delta P_{WTG} = \frac{k_{WTG}}{1 + sT_{WTG}} \tag{10}$$

where k_{WTG} and T_{WTG} are the gain constant and time constant of the WTG.

E. PHOTOVOLTAIC POWER GENERATOR

Malaysia typically receives monthly solar radiation of approximately 400–600 MJ/m^2 from the sun [33]. Crystalline or thin-film panels are used widely in Photovoltaic (PV) power plants to convert sunlight into electricity. This study assumed the PV generating system operates in a maximum power point tracking mode. The PV output power can be represented as [37]:

$$P_{solar} = A \times \eta_{solar} \times I \times [1 - (0.005\, T_a + 0.125)] \tag{11}$$

where P_{solar} is the output power of the PV system in Watt; A is the area of the cells (m^2); η_{solar} is the efficiency of the conversion from sunlight to electricity; I is the isolation (Watt/m2), and T_a is the ambient temperature in ^oC.

The transfer function of the PV power generator can be written as follows:

$$\Delta P_{PV} = \frac{k_{PV}}{1 + sT_{PV}} \tag{12}$$

where ΔP_{PV} is the output power of the PV; k_{PV} and T_{PV} are the gain constant and time constant of the photovoltaic cell behaviour.

F. ENERGY STORAGE SYSTEM

ESS has indeed gained significant attention in recent years as a means to enhance the frequency response of

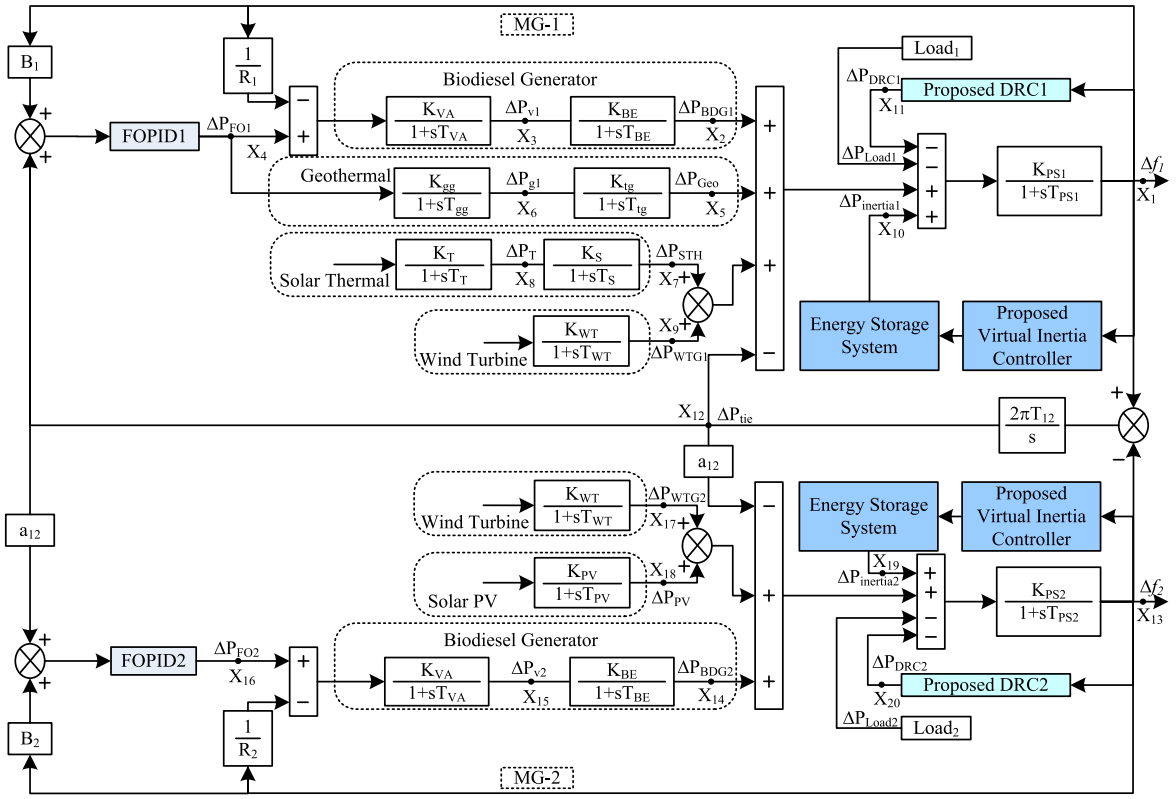

FIGURE 2. Dynamic model of MMG integrated with RESs.

MGs. By quickly responding to imbalances between power generation and demand, ESS can help reduce frequency deviation and contribute to system stability. Lithium-ion batteries are the most common type of battery used in LFC power applications due to their properties [38]. It can be rapidly charged and discharged and has a relatively long cycle life, both of which have significance for LFC. The proposed control technique in this paper is designed to keep the ESS unit fully charged during normal operating conditions and then automatically inject the system with the required active power during the contingencies. The transfer function of the ESS can be written as a first-order lag:

$$\Delta P_{ESS} = \frac{\Delta\,(P_{ch} - P_{des}\,)}{\Delta\omega} = \frac{K_{ESS}}{1 + T_{ESS}} \tag{13}$$

where ΔP_{ESS} is the output power of the ESS; K_{ESS} is the gain constant of the ESS; T_{ESS} is the time constant of the ESS.

G. PROPOSED FRACTIONAL DERIVATIVE VIRTUAL INERTIA CONTROL

This section demonstrates a novel design of the FDVIC based on the ESS proposed in this study. The objective of this design is to provide inertia and damping impact instantly during high penetration of RESs into the MGs. Short-term ESS, an inverter, and the proposed inertia controller can prove this concept. FDVIC controller operates separately from other control units in the model, such as the primary control loop

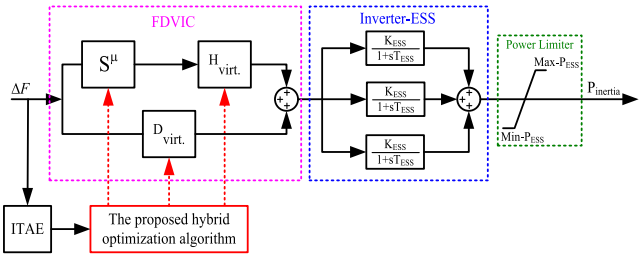

FIGURE 3. The proposed fractional derivative virtual inertia control system.

(droop control) and secondary control loop. As a result, the ESS's energy is completely exploited to enhance stability. The dynamic structure of the proposed FDVIC is presented in Fig. 3:

The dynamic equation of the proposed FDVIC controller design can be presented as follows

$$\Delta P_{\text{inertai i,j}} = \Delta f_{i,j}\left(s^{\mu v_{i,j}} H_{\text{vir. i,j}} + D_{\text{vir. i,j}}\right)\left[\frac{K_{ESS}}{1 + sT_{ESS}}\right] \tag{14}$$

where $\Delta P_{\text{inertiai,j}}$ is the change of active power supported to the $MG_{i,j}$ ($i \neq j$); $s^{\mu v_{i,j}}$ is the fractional derivative; μv is the derivative coefficient factor; $H_{\text{vir.i,j}}$ is the virtual inertia constant; $D_{\text{vir.i,j}}$ is the virtual damping coefficient constant;

K_{ESS} is the gain constant of the inverter based ESS; and T_{ESS} is the time constant of the inverter based ESS.

The FDVIC controller can control the power direction of the ESS. The proposed algorithm has been used in this paper to tune the value of μv and estimate the optimal value of $H_{vir.}$ and D_{vir}. To include the FDVIC controller impact with the dynamic swing power equation. Equation (4) can be modified as follows:

$$\Delta P_m - \Delta P_l \pm \Delta P_{inertia} = 2H\frac{d\Delta f}{dt} + D\Delta f \quad (15)$$

H. DEMAND RESPONSE CONTROLLER

Demand Response Controller (DRC) unit is used to improve system frequency, reduce operational costs, and increase the flexibility of the MGs to deal with the fluctuation and uncertainty of the RESs [9]. The conventional dynamic response in (4) will be modified to (16) to include the DRC loop, where ΔP_{DRC} is the change in the DRC active power. Based on the sign (negative or positive) of the frequency deviation, the binary indicator factor x_{DRC} is activated (1) or deactivated (0).

$$\Delta P_m - \Delta P_{load} \pm x_{DRC}\Delta P_{DRC} = 2H\frac{d\Delta f}{dt} + D\Delta f \quad (16)$$

In contrast to conventional control, such as adjusting the position of a valve or gate, DR control is known for its quick response to frequency regulation. In DR, the frequency threshold (Δf_{th}) and appliance shutoff time (T_{off}) are the two most critical factors to determine [39]. The number of electrical devices that require turning off is dependent on the following (17), as shown at the bottom of the next page, where Δf_{db} is the dead band frequency for the primary frequency control; Δf_{prm} is the MG's frequency deviation at the end of all primary control reserves delivered.

Assume there are a number (n) of appliances that will be chosen to participate in improving the frequency deviation of the proposed MGs. These appliances will be arranged according to priorities. The controller is designed to switch off the least important devices first. $P_1, P_2, \ldots P_k$ represents the individual power demands of the listed DR devices. The Δf_{th} parameter can be calculated for the ith appliance by:

$$\Delta f_{th(i)} = \Delta f_{db} - \left[\frac{\Delta f_{db} - \Delta f_{prm}}{P_{DRC}} \cdot \sum_{k=1}^{i} P_k\right] \quad (18)$$

The aggregated DR's frequency response characteristics are illustrated in Fig. 4.

In order to avoid quick switching, the responsive DR appliances (which are turned off because of the frequency deviation) cannot be turned back on before the minimum off-time has elapsed. After that, the responsive DR appliances are progressively turned on if the minimum off-time has elapsed and the frequency has been returned to the nominal value [40]. The assumed rate of reduction is k_{res} p.u. per second for the responsive DR load. The parameter T_{off} of the ith appliances can be calculated in (19):

$$T_{off\,(i)} = T_{off\,0} + \frac{1}{k_{res}} \sum_{k=1}^{i} P_k \quad (19)$$

where T_{off0} is the first switched minimum off-time of the DR appliance. The value of the k_{res} is evaluated by using the proposed algorithm. The overall control process of the DR controller to reduce the frequency deviation of the proposed MGs can be demonstrated in four steps as follows:

Step 1: In the first step, all DR appliances are in standby condition. If the system frequency drops below the dead band frequency, then go to step 2.

Step 2: In this step, DR appliances are progressively switched off. By using the formula in (17), the DR load that will be shed can be estimated. When the system frequency reduces to the nadir frequency, T_{off0} will initialize and go to step 3.

Step 3: If the T_{off0} is elapsed and $\Delta f > \Delta f_{db}$, then go to step 4. If $\Delta f < \Delta f_{db}$, go to step 2.

Step 4: At this step, the responding DR appliances have been managed and are being gradually recovered (turned back on). By using the rate of reduction k_{res}, the DR load will be reduced until all appliances are recovered. If $P_{DRC} = 0$, then go to step 1. If the $\Delta f < \Delta f_{db}$, go to step 3.

The dynamic structure of the proposed DR controller combined is illustrated in Fig. 5:

where P_{cf} is the demand contribution factor, and M_{DRi} is the intervention coefficient.

The proposed hybrid optimization algorithm has been utilized to determine the optimal values for both the demand contribution factor and the intervention coefficient. P_{cf} plays a pivotal role in controlling the gain of active power within the DRC, contributing significantly to its enhanced performance.

The final frequency deviation equation of the MG1 and MG2 has been derived by taking into consideration the relationship between the DGs of the MG integrated with RESs and including the proposed FDVIC technique with the DRC technique and the demand load of the proposed model depicted in Fig. 2 as follows:

$$\Delta f_1 = \frac{kps_1}{D_1 + 2H_1 s} \times [\Delta P_{BDG1} + \Delta P_{RES1} \pm \Delta P_{DRC1} \pm \Delta P_{inetial} - \Delta P_{loadl}] \quad (20)$$

where $\Delta P_{RES1} = \Delta P_{Geo} + \Delta P_{STH} + \Delta P_{WTG1}$

$$\Delta f_2 = \frac{kps_2}{D_2 + 2H_2 s} \times [\Delta P_{BDG2} + \Delta P_{RES2} \pm \Delta P_{DRC2} \pm \Delta P_{inetia\,2} - \Delta P_{load\,2}] \quad (21)$$

where $\Delta P_{RES2} = \Delta P_{WTG2} + \Delta P_{PV}$

where kps_1 and kps_2 are the gain constant of the MG power systems.

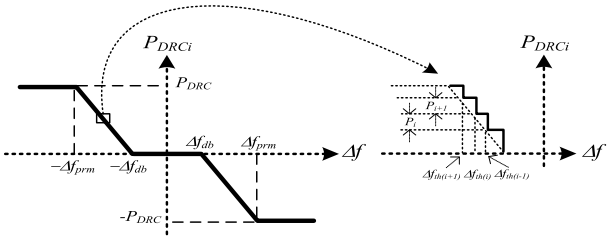

FIGURE 4. Frequency response behaviour of aggregate DRC.

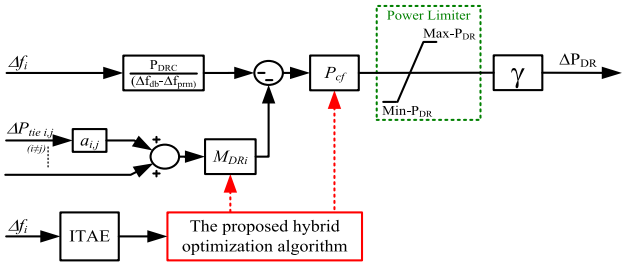

FIGURE 5. The proposed demand response control system.

The frequency response of the proposed MGs model at steady-state can be represented as in (22) [41]:

$$\Delta f_{ss} = \frac{\Delta P_{gen,ss} \pm \Delta P_{inertia,ss} \pm \Delta P_{DR,ss} - \Delta P_{load}}{D + \frac{1}{R}} \quad (22)$$

where Δf_{ss} is the frequency deviation at steady-state; $\Delta P_{gen,ss}$ is the change of the total power generated from the BDG and the RESs; $\Delta P_{inertia,ss}$ is the change of the active power supported from ESS; $\Delta P_{DR,ss}$ is the change in demand response power.

The steady-state frequency deviation in (22) can be minimized to zero if one or more of the three powers ($\Delta P_{gen,ss}$, $\Delta P_{inertia,ss}$, and $\Delta P_{DR,ss}$) are adequately available to balance the change in demand load ΔP_{load}. Therefore, $\Delta P_{inertia,ss}$, and $\Delta P_{DR,ss}$ are indicated to be used to regulate the frequency deviation in addition to the secondary control loop.

In order to improve the frequency performance in contingency situations, the proposed control strategy has the freedom to decide the optimal power sharing from each control loop. If the shares power of $P_{inertia}$, P_{DR}, and $P_{gen.}$ are δ, γ, and ξ, respectively, then:

$$\xi = 1 - \delta + \gamma \quad (23)$$

If the total sharing power to balance the change in the demand load is ΔP_{total}, then the power contribution from ESS is:

$$\Delta P_{inertia} = \delta \Delta P_{total} \quad (24)$$

The power contribution of the DRC is present as follows:

$$\Delta P_{DR} = \gamma \Delta P_{total} \quad (25)$$

The value of γ acts as a pivotal control parameter for the demand response controller, determining its operation in tandem with FDVIC and FOPID by incorporating adjustments based on a predefined percentage.

Finally, the power contribution by the conventional generator integrated with RESs is:

$$\Delta P_{gen.} = (1 - \delta + \gamma)\Delta P_{total} \quad (26)$$

It should be noted that the steady-state values depend on the proportion between the conventional control loop (ξ), the DR control (γ), and the virtual inertia control (δ), which is decided by the system administrator in negotiations with consumers.

III. THE PROPOSED CONTROL STRATEGY

The closed-loop control technique of MMG can be simplified as depicted in Fig. 6:

FOPID controller transfer function is given in (27) [42]:

$$T_{FOPD} = k_{pi} + \frac{k_{ii}}{s^{\lambda i}} + k_{di} s^{\mu i} \quad (27)$$

where k_{pi}, k_{ii}, and k_{di} are proportional, integral, and derivative parameters of FOPID, λ_i, and μ_i represent the fractional-order operators and their values tuned in the range (0,1).

In this work, two FOPID controller units have been used in the secondary control loop of the proposed model. Its value is tuned using the hybrid SSAMGO algorithm. Furthermore, in order to provide the proposed model with the required virtual inertia and virtual damping, new FDVIC techniques have been designed to operate independently in low inertia situations. The transfer function of the proposed FDVIC technique is presented as follows:

$$T_{P_{inetria\ i}} = H_{vir.\ i} s^{\mu vi} + D_{vir.\ i} \quad (28)$$

where $H_{ver.i}$, $D_{ver.i}$, and μvi tuned by using the proposed hybrid algorithm.

The DR control loop transfer function is given as:

$$T_{DRC} = M_{DRi} + P_{cfi} \quad (29)$$

where M_{DRi} is the primary DR control coefficient; P_{cfi} is the secondary DR control coefficient.

$$P_{DRC} = \begin{cases} -P_{DRC} & \text{if } \Delta f > \Delta f_{pm} \\ -\frac{P_{DRC}}{(\Delta f_{db} - \Delta f_{pmm})}(\Delta f_{db} - \Delta f) & \text{if } \Delta f_{db} \le \Delta f \le \Delta f_{prm} \\ 0 & \text{if } -\Delta f_{db} < \Delta f < -\Delta f_{prm} \\ -\frac{P_{DRC}}{(\Delta f_{db} - \Delta f_{pmm})}(\Delta f - \Delta f_{db}) & \text{if } \Delta f_{prm} \le \Delta f \le \Delta f_{db} \\ P_{DRC} & \text{if } \Delta f < -\Delta f_{prm} \end{cases} \quad (17)$$

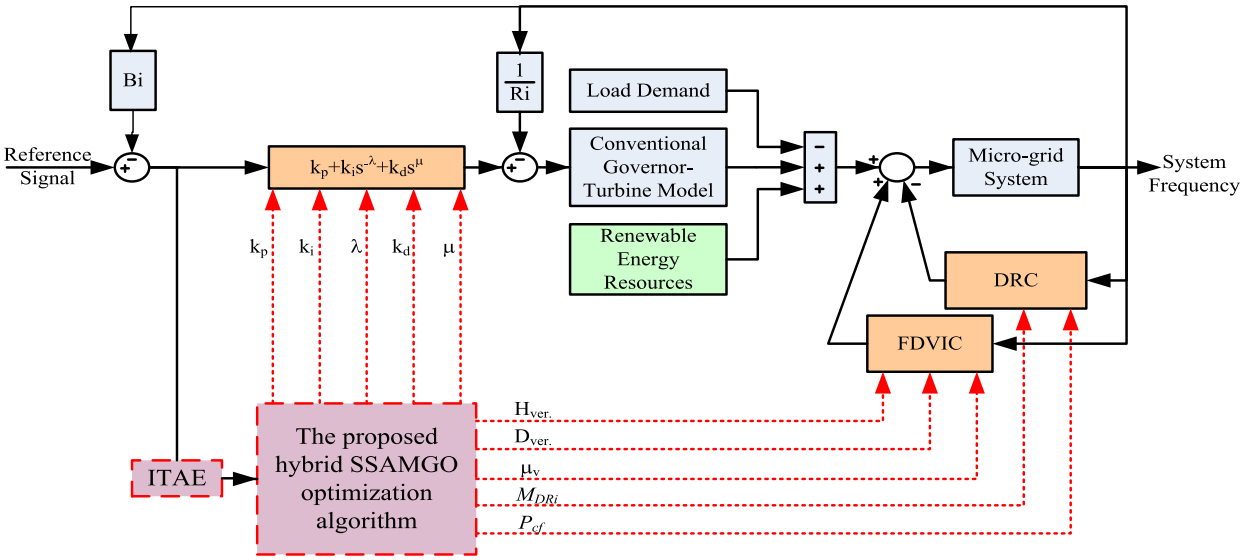

FIGURE 6. The proposed closed-loop control approach of the MMG.

The selection of the ITAE performance index for controller parameter design in this study is based on its superior performance compared to other indices [43]. Thus, the fitness function is given as:

$$\text{Min(J)} = \text{ITAE} = \int_0^t t\left\{\left|U_i + \Delta f_j + \Delta P_{tiei-j}\right|\right\} dt \quad i \neq j \tag{30}$$

where

$$U_i(t) = ACE_i \times \left(k_{pi} + \frac{k_{ii}}{s^{\lambda i}} + k_{di}s^{\mu i}\right)$$

and

$$ACE_i = \sum_i^N \Delta P_{tiei} + B_i \Delta f_i$$

where ACE_i is the area control error of the ith area; B_i is the system frequency bias in (p.u MW/Hz). Under the conditions of the following inequalities:

$k_p^{min} < k_{pi} < k_p^{max}$; $k_i^{min} < k_{ii} < k_i^{max}$
$k_d^{min} < k_{di} < k_d^{max}$; $\lambda^{min} < \lambda_i < \lambda^{max}$
$\mu^{min} < \mu_i < \mu^{max}$; $H_{vir.}^{min} < H_{vir.i} < H_{vir.}^{max}$
$D_{vir.}^{min} < D_{vir.i} < D_{vir.}^{max}$; $\mu v^{min} < \mu v_i < \mu v^{max}$
$M_{DR}^{min} < M_{DRi} < M_{DR}^{max}$; $P_{cf}^{min} < P_{cfi} < P_{cf}^{max}$

The maximum and minimum ranges used for tuning the parameters of the FOPID controller, such as k_p, k_i, and k_d are bounded between $[-100, -0.01]$, λ, and μ is selected between [0, 1].

IV. HYBRID SSAMGO OPTIMIZATION ALGORITHM

To obtain the optimal values of the three controller parameters (FOPID, FDVIC, and DRC) for a multi-MG power system, an effort was made to develop a new hybrid metaheuristic algorithm that combines the strengths of swarm-inspired algorithms such as SSA [44] with MGO. The Sparrow Search Algorithm (SSA) has limitations in terms of exploring new areas, resulting in poor performance in handling multi-dimensional and complex problems. From this point of view, the SSA is integrated with the territorial solitary males' tactic of MGO [45], [46] and the chaotic map mechanism in order to improve the exploration phase. It is worth noting that the newly discovered solutions' positions are included with the information on the best optimal solution to develop both the exploration phase and importing high-quality solutions at the same time. The improvements of the proposed hybrid algorithms can be presented as follows:

In (31) shows the improved SSA used in this work,

$$X_{i,j}^{t+1} = \begin{cases} X_{i,j}^t \times \exp\left(\frac{-i}{\alpha \cdot iter_{max}}\right) - X_{i,j}^t & R_2 < ST \\ X_{best}^{t+1} + M & R_2 \geq ST \end{cases} \tag{31}$$

$M = 4 \times (1 - m)$, $m = rand$, where m is chosen randomly between the range of [0, 1].

where t represents the current iteration; $j = 1, 2, 3, \ldots, n$; n presents the number of the variables that optimize; $X_{i,j}{}^t$ is the value of the jth dimension of the ith sparrow at t; $X_{best}{}^{t+1}$ is the best individual location; $iter_{max}$ is the maximum number of iterations. α is a random number between [0, 1]; R_2 is the alarm value chosen between [0, 1]; ST is the safety threshold value chosen between [0.5,1].

The discoverer location in (31) of SSA has been improved by including the information on neighbour solutions in the first phase of the equation when $R2 < ST$, while the chaotic map, along with the best optimal solutions found so far, has been applied in the second phase when $R2 \geq ST$. This improvement can significantly increase the exploration of the optimizer and prevent falling in local optima.

The first term of the follower's location of SSA has been improved by using the mechanism of solitary territorial

TABLE 1. Benchmark functions.

Function name		Type	Formula	Dimension (d)	Range
Sphere	F1	US	$f(x)=\sum_{i=1}^{d} x_i^2$	30	[-100, 100]
Schwefel 2.22	F2	UN	$f(x)=\sum_{i=1}^{d}\lvert x_i\rvert+\prod_{i=1}^{d}\lvert x_i\rvert$	30	[-10, 10]
Schwefel 2.26	F8	MS	$f(x)=-\sum_{i=1}^{d}\left(x_i \sin\left(\sqrt{\lvert x_i\rvert}\right)\right)$	30	[-500, 500]
Ackley	F10	MN	$f(x)=-20\exp\left(-0.2\sqrt{\frac{1}{d}\sum_{i=1}^{d} x_i^2}\right)-\exp\left(\frac{1}{d}\sum_{i=1}^{d}\cos 2\pi x_i\right)+20+e$	30	[-32, 32]
Penalized 2	F12	MN	$f(x)=0.1\left\{\begin{array}{l}\sin^2(3\pi x_1)+\sum_{i=1}^{d}(x_i-1)^2\left[1+\sin^2(3\pi x_i+1)\right]\\ +(x_d-1)^2\left[1+\sin^2(3\pi x_d)\right]\end{array}\right\}+\sum_{i=1}^{d} U(x_i,5,100,4)$	30	[-50, 50]

TABLE 2. Benchmark functions.

Function	Index	SSAMGO	SSAGWO	PSOGSA	MPSOGA	CPSO
F1	Best	0	1.1931×10^{-128}	42.7235	$3.5688\times10^{+04}$	$4.3911\times10^{+04}$
	Mean	0	9.1668×10^{-55}	308.3442	$6.6840\times10^{+04}$	$6.3669\times10^{+04}$
	Worst	0	1.8334×10^{-53}	842.9858	$8.0561\times10^{+04}$	$7.5209\times10^{+04}$
	STD	0	4.0995×10^{-54}	215.1169	$9.3496\times10^{+03}$	$6.8245\times10^{+03}$
F2	Best	1.5932×10^{-247}	7.5080×10^{-118}	2.9194×10^{-08}	$9.0956\times10^{+08}$	$2.8587\times10^{+05}$
	Mean	1.0861×10^{-204}	1.2279×10^{-30}	43.4564	$8.6502\times10^{+12}$	$3.7066\times10^{+09}$
	Worst	1.7743×10^{-203}	2.3915×10^{-29}	110.0510	$8.6146\times10^{+13}$	$1.9167\times10^{+10}$
	STD	0	5.3419×10^{-30}	45.6627	$2.3090\times10^{+13}$	$6.0154\times10^{+09}$
F8	Best	$-1.2569\times10^{+04}$	$-9.5402\times10^{+03}$	$-7.1072\times10^{+03}$	$-5.4177\times10^{+03}$	$-4.5621\times10^{+03}$
	Mean	$-1.1847\times10^{+04}$	$-8.4706\times10^{+03}$	$-6.2020\times10^{+03}$	$-5.4177\times10^{+03}$	$-3.9268\times10^{+03}$
	Worst	$-9.0163\times10^{+03}$	$-7.4124\times10^{+03}$	$-5.4715\times10^{+03}$	$-5.4177\times10^{+03}$	$-3.5715\times10^{+03}$
	STD	$1.4531\times10^{+03}$	556.6444	523.6907	9.3312×10^{-13}	231.9713
F10	Best	8.8818×10^{-16}	8.8818×10^{-16}	0.9313	19.9668	20.1562
	Mean	8.8818×10^{-16}	8.8818×10^{-16}	7.8574	19.9668	20.2579
	Worst	8.8818×10^{-16}	8.8818×10^{-16}	18.4607	19.9668	20.3541
	STD	0	0	5.7494	7.2900×10^{-15}	0.0565
F12	Best	1.2062×10^{-16}	1.0660×10^{-15}	7.7209	$2.3417\times10^{+08}$	$1.9415\times10^{+08}$
	Mean	4.0462×10^{-14}	7.2378×10^{-13}	12.2799	$5.9084\times10^{+08}$	$5.6059\times10^{+08}$
	Worst	3.5152×10^{-13}	5.2621×10^{-12}	19.5074	$7.7045\times10^{+08}$	$7.7634\times10^{+08}$
	STD	8.4222×10^{-14}	1.3653×10^{-12}	3.3100	$1.5266\times10^{+08}$	$1.3508\times10^{+08}$

males of the MGO. This mechanism is inspired by the battle between the adult male gazelles to take place over the territory or possession of the female, which is modelled in (32), as shown at the bottom of the page, where ri_1 and ri_2 are random integers values chosen 1 or 2; $X_{p^{t+1}}$ is the optimal location occupied by the producer; A is a matrix [1 x n] which each element inside assigned 1 or -1; $A^+ = A^T(AA^T)^{-1}$; L is a matrix [1 x n] which each element inside is 1; BH is the young male herd coefficient vector; more details about calculating the factors BH, F, and Cof_r please refer to [45].

V. SIMULATION RESULTS AND DISCUSSION

The dynamic response of the low-inertia MMG system integrated with RESs for the FOPID, FDVIC, and DRC controllers is described in this section. By using five benchmark functions, the proposed hybrid SSAMGO algorithm's performance is evaluated by comparing it with SSAGWO, PSOGSA, MPSOGA, and CPSO algorithms in terms of statistical findings. Furthermore, the proposed SSAMGO-tuned twenty parameters of the three loop controllers are analyzed for the MGs power system (i.e., five parameters for the FOPID controller of MG1, five parameters for the FOPID controller of MG2, three parameters for the FDVIC of MG1, three parameters for the FDVIC of MG2, two parameters for the DRC of MG1, and two parameters for the DRC of MG2). The MG model is developed and implemented using MATLAB/Simulink.

A. VALIDATION OF BENCHMARK FUNCTIONS

The performance of the SSAMGO algorithm is evaluated against SSAGWO, PSOGSA, MPSOGA, and CPSO algorithms using five benchmark functions with diverse

$$X_{i,j}^{t+1}=\left\{\begin{array}{ll} X_{ibest}^{t+1}-\lvert(ri_1\times BH-ri_2\times X(t))\times F\rvert\times Cof_r & \text{if } R_2<ST\\ X_P^{t+1}+\left\lvert X_{i,j}^{t}-X_P^{t+1}\right\rvert\cdot A^+\cdot L & \text{otherwise}\end{array}\right\} \quad (32)$$

TABLE 3. Virtual inertia and virtual damping for FDVIC of MG1 and MG2.

Optimization Algorithm Technique	FDVIC-1 (MG1)			FDVIC-2 (MG2)		
	H_{vir-1}	D_{vir-1}	μ_1	H_{vir-2}	D_{vir-2}	μ_2
SSAGWO-FDVIC	3.5230	4.8590	0.0125	3.6670	4.5670	0.0136
PSOGSA-FDVIC	2.1948	1.7349	0.1146	1.9329	2.4386	0.1298
MPSOGA-FDVIC	2.3310	2.6319	0.3571	1.9850	2.1350	0.5682
CPSO-FDVIC	2.3565	2.7523	0.7752	1.7536	2.2354	0.2704
SSAMGO-FDVIC	1.2110	1.4320	0.6326	1.1210	1.3250	0.5001

characteristics. This comparison provides a comprehensive assessment of the effectiveness of these algorithms [47], [48]. The evaluation of hybrid SSAMGO algorithms involves benchmark functions detailed in Table 1. Specifically, F1 and F2 are categorized as unimodal with a single global best solution (''U''). The table further distinguishes the separability of these functions, using ''S'' for separable and ''N'' for non-separable characteristics. Algorithm exploitation ability is assessed using unimodal benchmark functions, indicating the algorithm's proficiency in local search. F8, F10, and F12 denote multimodal functions. These functions, with multiple global best solutions, assess an algorithm's exploration capability. Table 1 categorizes functions labelled with ''M'' as multimodal, further classifying them as separable or non-separable [49]. Table 2 summarizes statistical results from algorithms on classical benchmarks, comparing mean and standard deviation (SD) for best and worst outcomes. Experiments conducted independently with 20 runs per algorithm, used recorded results for evaluation. Benchmark functions were assessed with a fixed population size of 30 and 500 iterations. From Table 2, SSAMGO shows significant enhancements in the exploration and exploitation phases. Fig. 7 displays the convergence curves for SSAMGO, SSAGWO, PSOGSA, MPSOGA, and CPSO, underscoring its superior performance in tackling optimization challenges posed by benchmark functions.

B. TIME DOMAIN ANALYSIS OF THE MMG POWER SYSTEM

In this subsection, the virtual inertia constant and virtual damping coefficient have been estimated by using the proposed SSAMGO and compared with other hybrid optimization techniques. Table 3 illustrates the optimal value of the H_{vir}, D_{vir}, and μ for the FDVIC of MG1 and MG2, respectively. The results show that the value of the virtual inertia and virtual damping when using SSAMGO is less than other optimization techniques by (65.62%, 44.82%, 48.05%, and 48.61%) for H_{vir1} and (70.53%, 17.46%, 45.60%, and 47.97%) for D_{vir1} and (69.43%, 42.00%, 43.53%, and 36.07%) for H_{vir2} and (70.99%, 45.66%, 37.94%, and 40.73%) for D_{vir2}. The estimated value of the virtual inertia constant has a very significant impact on the size of the capacity of the ESS that is used to support the MG power system with instant active power to reduce the value of the frequency nadir. In other words, the minimum value of the virtual inertia constant means reducing the size of the battery and leading to a reduction in the cost.

The proposed MG model is simulated under two scenarios. The first scenario shows the effect of the proposed new FDVIC technique on the dynamic performance of the MGs. In addition, proves the effectiveness of the proposed MG model under uncertainty in the load, variable virtual inertia, variable virtual damping, variable nominal load, uncertainties due to input real power of the solar PV and wind turbine generator RESs. At the same time, the second scenario demonstrates the dynamic performance of the MG power system after combining the proposed DRC technique with the FDVIC on the system frequency deviations and the stress on the ESS.

The time domain response analysis of the MG is presented as follows. MG1 consists of a biodiesel generator integrated with a geothermal power station, solar thermal power station, and wind turbine generator renewable energy sources. While MG2 consists of a biodiesel generator integrated with solar PV and wind turbine generator RESs. Fractional derivative virtual inertia control is used to control the active power support from the ESS to compensate for the lack of microgrid inertia in MG1 and MG2, respectively. A step load change of 0.12 p.u. (240 kW) and 0.1 p.u. (150 kW) of the rated power occurs in MG1 and MG2, respectively. Table 4 presents the optimized values of the FOPID controller using the proposed SSAMGO, in comparison with other hybrid optimization algorithms, for the MMG power system in both the first and second scenarios.

THE FIRST SCENARIO:

In this section, the impact of the proposed FDVIC technique on the dynamic performance of MGs is demonstrated.

1) DYNAMIC PERFORMANCE COMPARATIVE

To provide further evidence of the superior performance of the SSAMGO algorithm in optimizing the FOPID and FDVIC parameters for MG1 and MG2, a comprehensive comparison was conducted with several widely used meta-heuristic hybrid algorithms found in the existing literature.

The algorithms considered for this comparison included SSAGWO, PSOGSA, MPSOGA, and CPSO. These algorithms were employed to optimize the parameters of the FOPID and FDVIC controllers in the multi-MG model integrated with high penetration RESs, as discussed in the

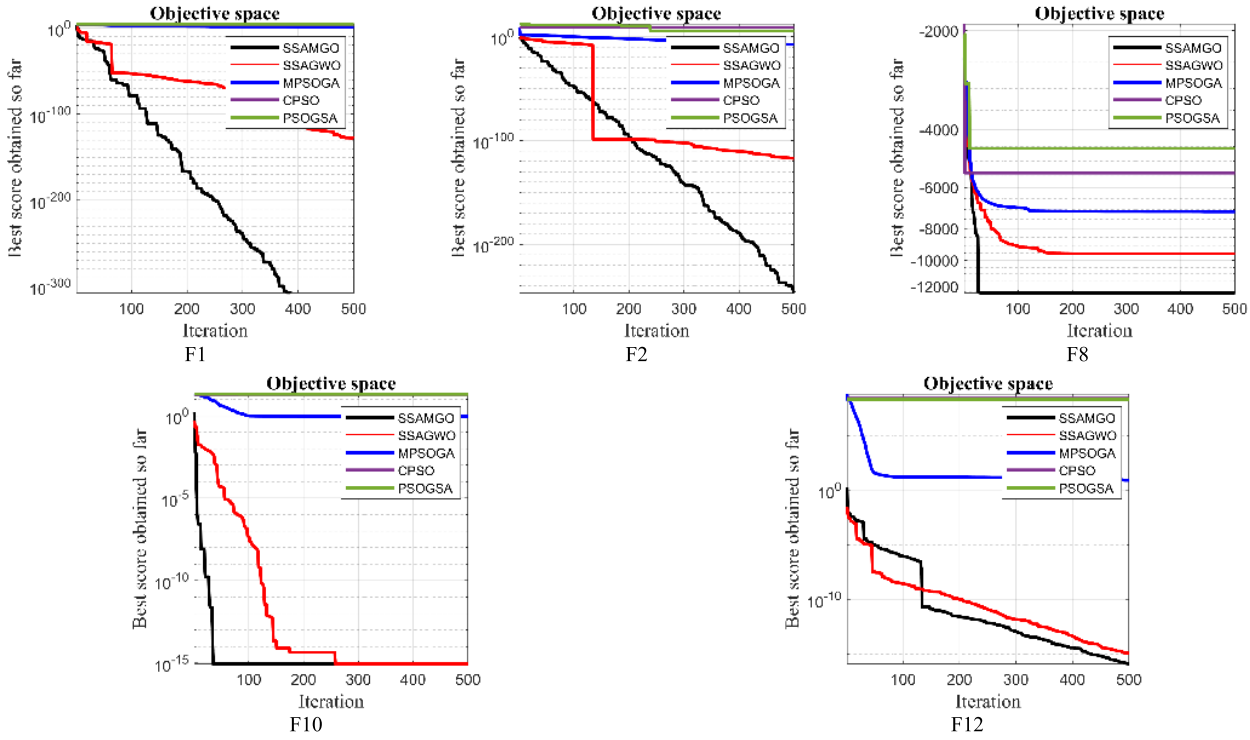

FIGURE 7. Convergence characteristics for the proposed SSAMGO compared with other hybrid optimization algorithms.

first scenario. By comparing the results obtained from the SSAMGO algorithm with those obtained from the other algorithms, we aimed to validate the effectiveness and superiority of the SSAMGO approach in achieving optimal parameter settings for the given system. To maintain fairness in the comparison, all algorithms were implemented in MATLAB, utilizing a system configuration consisting of an Intel Core i7 7th generation processor and 8 GB of RAM. In order to create a consistent evaluation framework, the maximum number of iterations and the population size were uniformly set to 100 and 30, respectively, for all the algorithms being compared. By establishing these standardized parameters, we ensured that each algorithm was assessed under the same computational conditions when optimizing the FOPID and FDVIC controller parameters for the multi-MG model incorporating high penetration RESs. Fig. 8, illustrates the frequency deviation of the proposed SSAMGO for tuning FOPID controller parameters for the secondary control loop of the MG1 and MG2 and for tuning FDVIC parameters of the MG1 and MG2 compared with (SSAGWO, PSOGSA, MPSOGA, and CPSO) hybrid optimization algorithms.

The results of the frequency deviation of MG1 and MG2 and the change of the tie line power are presented in Table 5. It is clear from Fig. 8 and the results illustrated in Table 5 that Settling Time (ST), Steady-State Error (SSE), Undershoot (US), and Best Score (BS) for the proposed SSAMGO algorithm optimized FOPID and FDVIC are much faster than other optimization-tuned FOPID and FDVIC controllers. ET, and ITAE are elapsed time, and integrated time absolute error performance index, respectively.

The ST of the SSAMGO tuned the FOPID and tuned the proposed FDVIC for the frequency response of MG1 is improved by (24.68%, 46.20%, 7.52%, and 61.01%) and for the frequency deviation of MG2 enhanced by (42.59%, 47.71%, 61.18%, and 72.67%) and for the change in the tie line power ameliorated by (40.45%, 4.85%, 75.04%, and 57.49%) from SSAGWO, PSOGSA, MPSOGA, and CPSO, respectively. Moreover, the SSE of the frequency deviation of the SSAMGO for MG1 is better than other hybrid optimization techniques by (72.56%, 98.18%, 98.73%, and 6.67%) and for frequency response of MG2 raises by (75.47%, 98.29%, 98.92%, and 7.14%) and for the tie line power deviation improved by (73.91%, 93.75%, 98.75%, and 33.33%), respectively. Furthermore, the proposed FDVIC technique in this work reduces the US of the frequency deviations, which has a significant impact on the frequency nadir and system stability, and it is enhanced by (105.76%, 144.23%, 19.23%, and 7.69%) than the other optimization techniques used to tune FDVIC parameters. Moreover, there is a significant enhancement in the steady-state values of the performance indices for frequency deviations and the change in tie-line power. Specifically, for the frequency deviation of the MG1, improvements are observed: 60.74% for ITAE, 2.63% for IAE, 12.5% for ISE, and 7.89% for

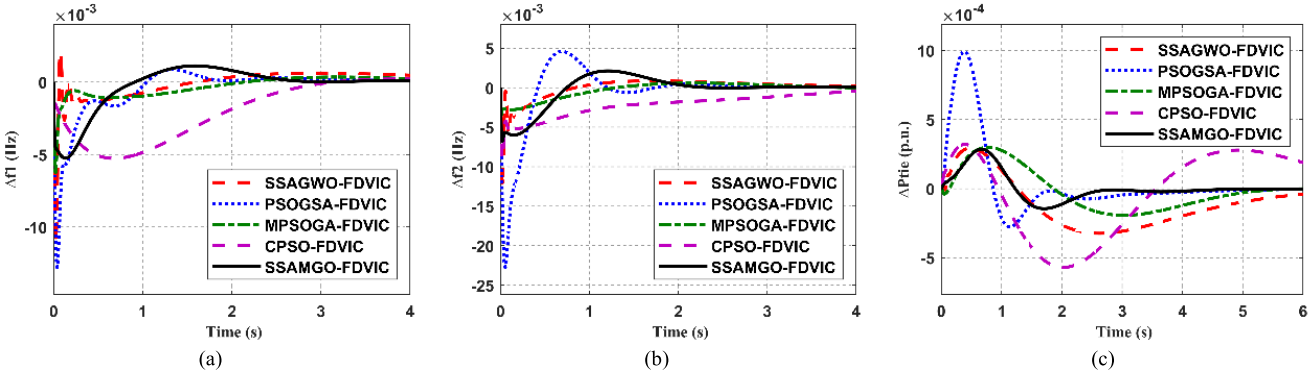

FIGURE 8. The dynamic response of the proposed algorithm compared to other optimization techniques for tuning FOPID controller parameters and FDVIC parameters: (a) The frequency deviation of MG1; (b) The frequency deviation of MG2; (c) The power deviation of the tie line.

TABLE 4. FOPID controller parameters for MMG.

Optimization Algorithm Technique	k_p	k_d	μ	k_i	λ	Execution Time (s)
SSAGWO-MG1	-50.2456	-52.5241	0.2832	-48.2465	0.5710	15536.9
SSAGWO-MG2	-35.1550	-0.0156	0.0100	-49.9990	0.9990	15536.9
PSOGSA-MG1	-4.2541	-11.0444	0.0568	-79.1746	0.7746	7353.7
PSOGSA-MG2	-5.7592	-7.7631	0.0105	-50.1111	0.7634	7353.7
MPSOGA-MG1	-93.4000	-16.2695	0.5598	-91.3346	0.5889	6857.6
MPSOGA-MG2	-1.5502	-53.2872	0.4307	-79.6204	0.9761	6857.6
CPSO-MG1	-10.0000	-2.4455	0.9886	-7.9373	0.9990	8239.9
CPSO-MG2	-10.0000	-7.1898	0.0768	-10.0000	0.9990	8239.9
SSAMGO-MG1	-4.9727	-19.8355	0.2621	-79.9185	0.9981	6640.9
SSAMGO-MG2	-9.9983	-19.9996	0.2077	-79.9151	0.9609	6640.9

TABLE 5. Frequency deviation and the change in tie line power of MG1 and MG2 of the first scenario.

Optimization Algorithm Technique	ST (s)	SSE	US	BS	ET (s)	ITAE	IAE	ISE	ITSE
				Δf_1					
SSAGWO-FDVIC	5.55	5.1×10^{-7}	107×10^{-4}	34.2×10^{-3}	15536.9	10.7×10^{-3}	3.8×10^{-3}	11.2×10^{-6}	3.8×10^{-6}
PSOGSA-FDVIC	7.77	77×10^{-7}	127×10^{-4}	23.0×10^{-3}	7353.7	23.6×10^{-3}	4.5×10^{-3}	1.5×10^{-5}	3.9×10^{-6}
MPSOGA-FDVIC	4.52	110×10^{-7}	62×10^{-4}	28.0×10^{-3}	6857.6	25.8×10^{-3}	3.9×10^{-3}	14.3×10^{-6}	4.2×10^{-6}
CPSO-FDVIC	10.72	1.5×10^{-7}	56×10^{-4}	47.2×10^{-3}	8239.9	21.5×10^{-3}	9.8×10^{-3}	3.4×10^{-5}	3.2×10^{-5}
SSAMGO-FDVIC	4.18	1.4×10^{-7}	52×10^{-4}	5.30×10^{-3}	6640.9	4.2×10^{-3}	3.7×10^{-3}	9.8×10^{-6}	3.5×10^{-6}
				Δf_2					
SSAGWO-FDVIC	3.78	5.3×10^{-7}	120×10^{-4}	34.2×10^{-3}	15536.9	8.3×10^{-3}	4.9×10^{-3}	7.9×10^{-6}	3.4×10^{-6}
PSOGSA-FDVIC	4.15	76×10^{-7}	227×10^{-4}	23.0×10^{-3}	7353.7	24.4×10^{-3}	7.8×10^{-3}	6.7×10^{-6}	7.3×10^{-6}
MPSOGA-FDVIC	5.59	120×10^{-7}	34×10^{-4}	28.0×10^{-3}	6857.6	26.4×10^{-3}	5.7×10^{-3}	4.3×10^{-6}	2.6×10^{-6}
CPSO-FDVIC	7.94	1.4×10^{-7}	90×10^{-4}	47.2×10^{-3}	8239.9	26.9×10^{-3}	10.5×10^{-3}	2.8×10^{-5}	2.5×10^{-5}
SSAMGO-FDVIC	2.17	1.3×10^{-7}	67×10^{-4}	5.30×10^{-3}	6640.9	4.6×10^{-3}	4.8×10^{-3}	1.6×10^{-6}	1.7×10^{-6}
				ΔP_{tie}					
SSAGWO-FDVIC	7.91	2.3×10^{-7}	3.2×10^{-4}	34.2×10^{-3}	15536.9	3.7×10^{-3}	1.2×10^{-3}	2.6×10^{-7}	6.6×10^{-7}
PSOGSA-FDVIC	4.95	9.6×10^{-7}	2.7×10^{-4}	23.0×10^{-3}	7353.7	3.2×10^{-3}	0.8×10^{-3}	4.3×10^{-7}	2.1×10^{-7}
MPSOGA-FDVIC	18.87	48×10^{-7}	1.9×10^{-4}	28.0×10^{-3}	6857.6	11.1×10^{-3}	1.1×10^{-3}	1.4×10^{-7}	3.3×10^{-7}
CPSO-FDVIC	11.08	0.9×10^{-7}	5.6×10^{-4}	47.2×10^{-3}	8239.9	7.9×10^{-3}	1.9×10^{-3}	5.9×10^{-7}	1.6×10^{-6}
SSAMGO-FDVIC	4.71	0.6×10^{-7}	1.4×10^{-4}	5.30×10^{-3}	6640.9	0.7×10^{-3}	0.3×10^{-3}	5.8×10^{-8}	5.3×10^{-8}

ITSE. For frequency deviation of MG2, enhancements are noted: 44.57% for ITAE, 2.04% for IAE, 62.79% for ISE, and 34.62% for ITSE. Similarly, for the change in tie-line power, considerable advancements are registered: 78.12% for ITAE, 62.5% for IAE, 58.47% for ISE, and 74.76% for ITSE. These results show that the studied MG has improved its load-frequency characteristic as intended.

2) COMPARATIVE BETWEEN THE PROPOSED FDVIC AND CONVENTIONAL VIC

The frequency response of MG1 and MG2, as depicted in Fig. 9, demonstrates an improvement in dynamic performance. Specifically, the proposed FDVIC techniques enhance MG1 frequency undershoot by 40.37%, MG2 frequency undershoot by 66.62%, and tie line power undershoot

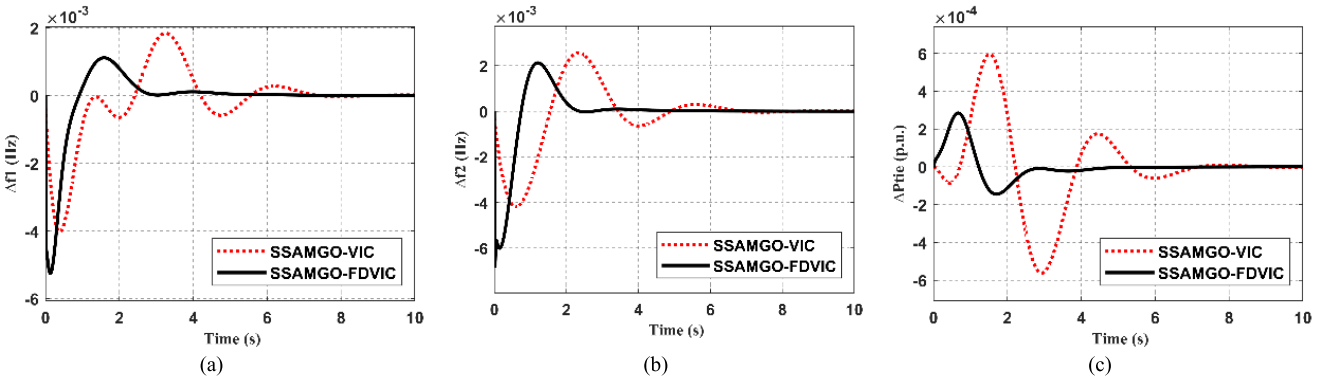

FIGURE 9. The dynamic response of the SSAMGO-tuned FDVIC compared with SSAMGO-tuned conventional VIC: (a) The frequency deviation of MG1; (b) The frequency deviation of MG2; (c) The power deviation of the tie line.

TABLE 6. Frequency deviation and the change in tie line power of MG1 and MG2 of proposed FDVIC compared with VIC.

Optimization Algorithm Technique	Δf_1						
	ST (s)	RT (s)	SSE	OS	BS	ET (s)	ITAE
SSAMGO-VIC	7.01	227.5×10^{-6}	7.92×10^{-7}	18×10^{-4}	50.9×10^{-3}	11478.6	13.83×10^{-3}
SSAMGO-FDVIC	4.18	19.6×10^{-6}	1.47×10^{-7}	11×10^{-4}	5.3×10^{-3}	6640.9	4.19×10^{-3}
				Δf_2			
SSAMGO-VIC	6.50	57.0×10^{-6}	3.99×10^{-7}	25×10^{-4}	50.9×10^{-3}	11478.6	15.77×10^{-3}
SSAMGO-FDVIC	2.17	13.3×10^{-6}	1.38×10^{-7}	21×10^{-4}	5.3×10^{-3}	6640.9	4.57×10^{-3}
				ΔP_{tie}			
SSAMGO-VIC	6.90	2500×10^{-6}	1.68×10^{-7}	5.9×10^{-4}	50.9×10^{-3}	11478.6	3.967×10^{-3}
SSAMGO-FDVIC	4.71	680.2×10^{-6}	0.59×10^{-7}	2.8×10^{-4}	5.3×10^{-3}	6640.9	0.75×10^{-3}

TABLE 7. Frequency deviation and the change in tie line power of MG1 and MG2 of proposed FDVIC compared without VIC.

Optimization Algorithm Technique	Δf_1						
	ST (s)	RT (s)	SSE	OS	BS	ET (s)	ITAE
SSAMGO-without VIC	4.56	-107.78×10^{-4}	33×10^{-4}	3.48×10^{-7}	9.3×10^{-3}	6837.5	12.13×10^{-3}
SSAMGO-FDVIC	4.18	19.6×10^{-6}	1.47×10^{-7}	11×10^{-4}	5.3×10^{-3}	6640.9	4.19×10^{-3}
				Δf_2			
SSAMGO-without VIC	5.95	-239.01×10^{-4}	63×10^{-4}	3.69×10^{-7}	9.3×10^{-3}	6837.5	27.82×10^{-3}
SSAMGO-FDVIC	2.17	13.3×10^{-6}	1.38×10^{-7}	21×10^{-4}	5.3×10^{-3}	6640.9	4.57×10^{-3}
				ΔP_{tie}			
SSAMGO-without VIC	9.18	-7.99×10^{-4}	7.1×10^{-4}	1.44×10^{-7}	9.3×10^{-3}	6837.5	4.37×10^{-3}
SSAMGO-FDVIC	4.71	680.2×10^{-6}	0.59×10^{-7}	2.8×10^{-4}	5.3×10^{-3}	6640.9	0.75×10^{-3}

by 31.74% when compared to the conventional VIC technique under the same operating conditions. Furthermore, the proposed FDVIC techniques have also led to improvements in several performance metrics. The rise time (RT), SSE, overshoot (OS), and the steady-state value of ITAE of the frequency deviations, as well as the change in tie line power, have all shown enhancements. Moreover, the SSAMGO-tuned FDVIC technique requires less time to achieve optimal values compared to the SSAMGO-tuned conventional VIC technique. The elapsed time for obtaining the optimal values using the FDVIC approach is significantly shorter than that required by the conventional VIC technique. A comprehensive breakdown of these results can be found in Table 6.

3) DYNAMIC PERFORMANCE OF FDVIC

The proposed FDVIC technique implemented in an MG power system effectively emulates the behaviour of conventional synchronous generators, which possess inherent inertia. Fig. 10 depicts the comparison between using FDVIC to compensate MG with inertia and without using any technique for inertia controller. It is clear from the results that the FDVIC technique approach improves the transient response of the MG. Moreover, it reduces the frequency fluctuations and enhances the system's ability to handle the rapid change in power demand. The results demonstrated in Table 7 show that FDVIC has faster response times and reduces settling time by 8.33%, undershoot by 51.24%, and overshoot by 66.67% for the frequency of MG1. While

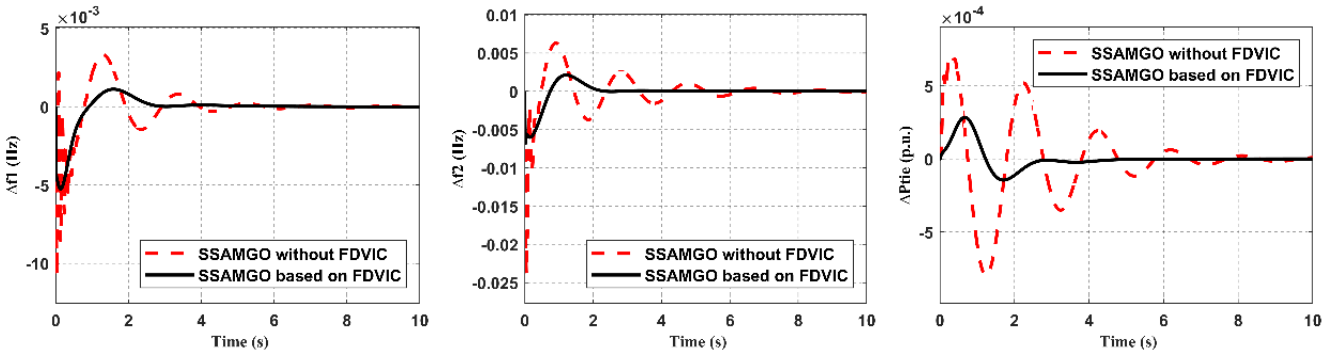

FIGURE 10. The dynamic response of the SSAMGO tuned FDVIC compared with SSAMGO without virtual inertia controller.

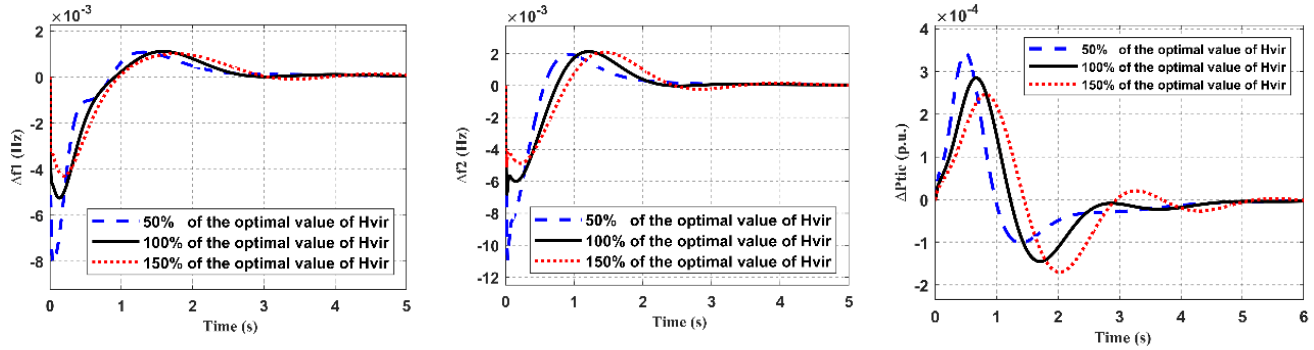

(a) (b) (c)

FIGURE 11. The dynamic response of the MG1 and MG2 under different virtual inertia constants (50% 150% from its optimal value): (a) The frequency deviation of MG1; (b) The frequency deviation of MG2; (c) The power deviation of the tie line.

reducing the ST, US, and OS by 63.52%, 71.53%, and 66.67% for the frequency of MG2, respectively.

Significant enhancements in frequency stability, transient responsiveness, and overall system stability result from incorporating the proposed virtual inertia control into an MG. It allows MG systems to function reliably and efficiently by reducing the challenges caused by renewable energy's lack of inherent inertia.

4) PERFORMANCE EVALUATION OF ESTIMATED VIRTUAL INERTIA AND VIRTUAL DAMPING

In the simulations mentioned above, the virtual inertia constant and the virtual damping coefficient are determined optimally using the SSAMGO algorithm for the FDVIC controller. In order to assess the robustness of the proposed FDVIC approach based on the SSAMGO algorithm, the values of the optimal H_{vir} and D_{vir} were varied within the range of 50% to 150%. The effectiveness of the controller is showcased by utilizing the FOPID controller parameters of MG1 and MG2 under normal operating conditions. The dynamic response of the MG with varying values of the virtual inertia constant is depicted in Fig. 11. Similarly, Fig. 12 displays the dynamic response of the MG when the virtual damping coefficient is changed.

Based on the observations from these figures, we can draw the conclusion that the proposed FDVIC controller, utilizing optimal values, exhibits robustness against uncertainties in the parameters. It effectively maintains the MG frequency and tie-line power at their reference values within short time intervals.

5) PERFORMANCE EVALUATION UNDER RANDOM LOAD DEMAND VARIATION

Fig. 13 demonstrates the application of a random step change in load demand to MG1, serving as a means to evaluate the effectiveness of the proposed SSAMGO compared with other hybrid optimization algorithms. To assess the system's response, Fig. 14 displays the frequency response of MG1, MG2, and tie-line power. This analysis aims to evaluate the performance of the proposed algorithm in maintaining system stability and regulating power distribution in response to load variations. Based on the findings, it is evident that the proposed algorithm exhibits faster tuning of the FOPID and FDVIC responses compared to other optimization techniques when subjected to sudden load changes. Furthermore, the tie-line power supplied by the system demonstrates the ability to adjust in response to varying load demands while maintaining a consistent output level. These results highlight the effectiveness of the proposed algorithm in dynamically

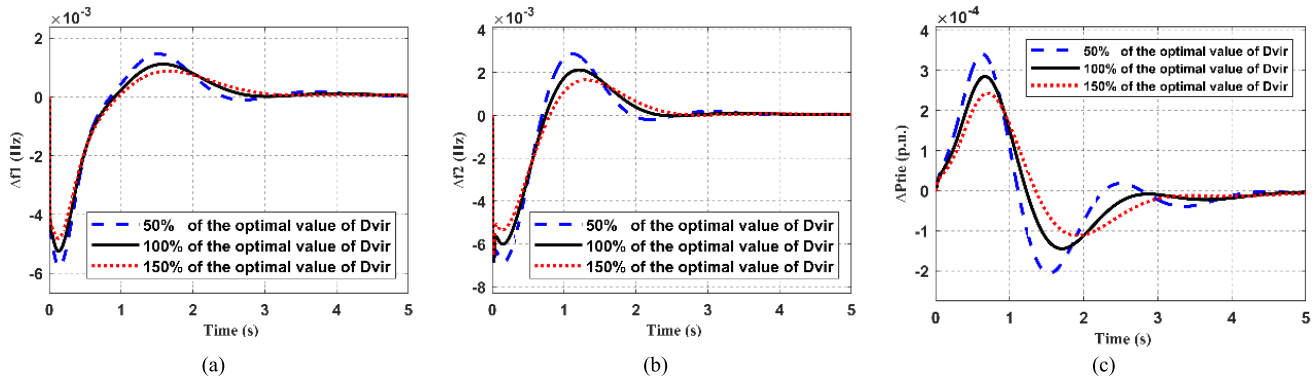

FIGURE 12. The dynamic response of the MG1 and MG2 under different virtual damping coefficients (50% 150% from its optimal value): (a) The frequency deviation of MG1; (b) The frequency deviation of MG2; (c) The power deviation of the tie line.

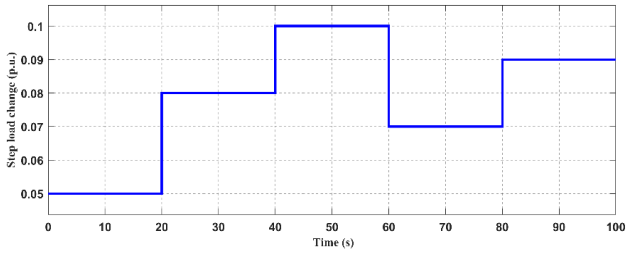

FIGURE 13. Random step change load demand.

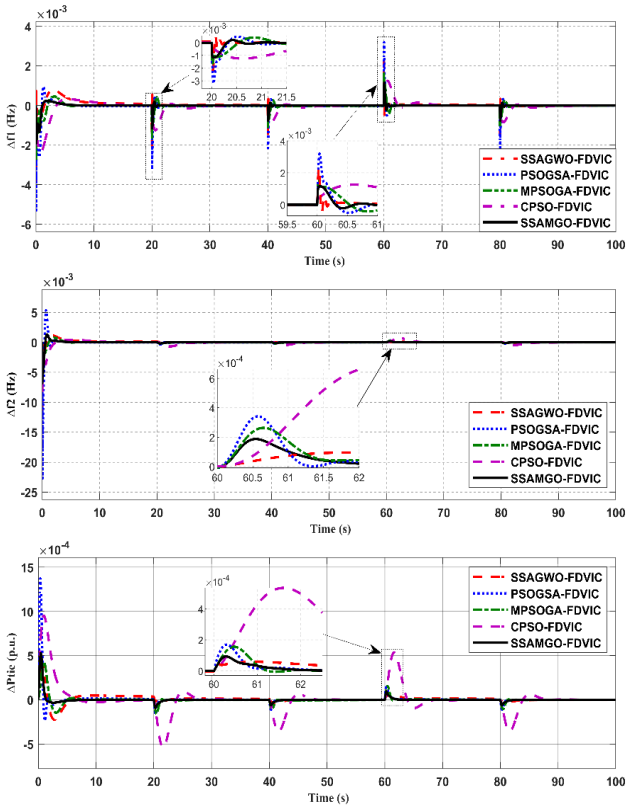

FIGURE 14. Dynamic response of MG1 and MG2 at a random change load.

adapting to changes in the system, ensuring stability and optimal performance.

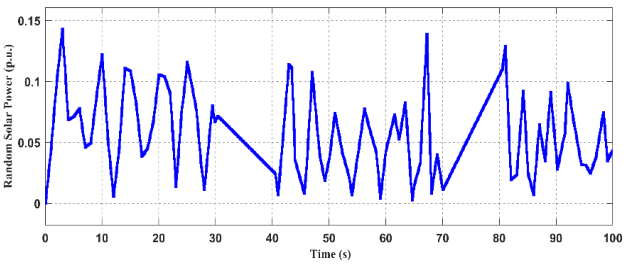

FIGURE 15. Real-time solar input power.

6) REAL-TIME VARIATION OF RESS PERFORMANCE EVALUATION

In this scenario, the case focuses on analyzing the variation in power output of solar PV units using real-time monthly average irradiance data collected from the Subang meteorological centre was specifically recorded at Universiti Putra Malaysia [42]. The data spans from January to December 2014 and comprises 200 time slots of 0.5 seconds each, as depicted in Fig. 15.

To assess the performance of the developed MMG model, real-time variations in solar power are tested. The dynamic response of the system is recorded and presented in Fig. 16, where the proposed SSAMGO algorithm is compared with other hybrid optimization algorithms. The results indicate that the SSAMGO-tuned parameters for the FOPID and FDVIC controllers exhibit superior and more consistent responses, characterized by minimal overshoot and undershoot. This finding suggests that the SSAMGO algorithm outperforms other tuning methods in achieving smoother and more efficient control of the MG system.

The Malaysian Meteorological Department in Kuala Terengganu collects real-time data on wind power variation by monitoring changes in wind speed throughout the year. The location of the department is specified by the coordinates 5°23' N latitude and 103°06' E longitude, with an elevation of 5.2 meters [50]. To evaluate the reliability of the controller, the wind power variation data is converted into seconds. Fig. 17 illustrates this process. Additionally,

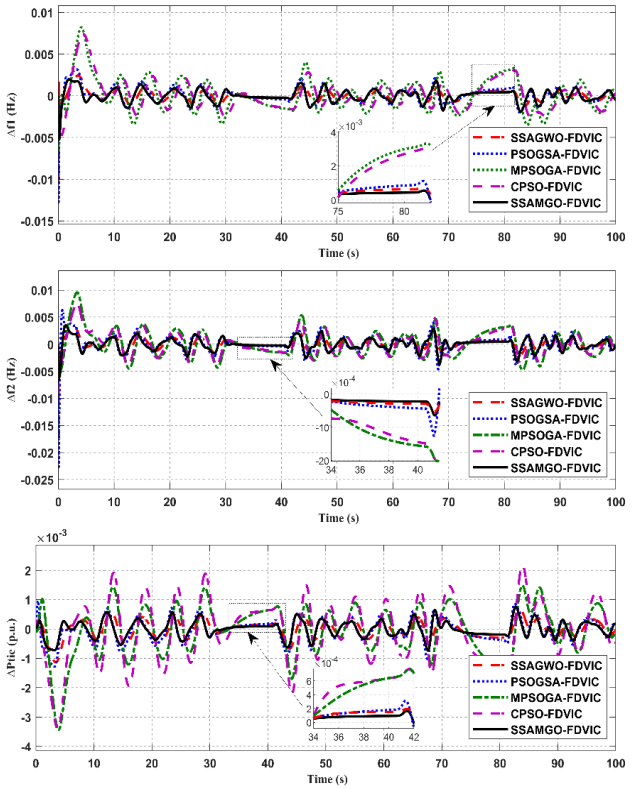

FIGURE 16. Dynamic response of the MMG power system under real-time solar input power.

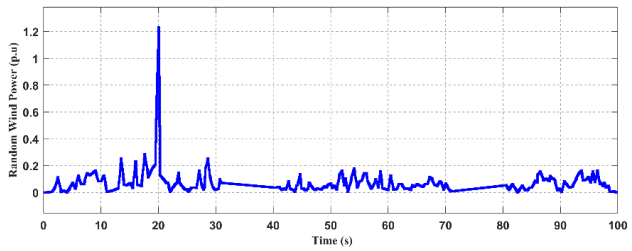

FIGURE 17. Real-time Wind-turbine Input Power.

Fig. 18 displays the frequency response and tie-line power deviation resulting from the aforementioned wind power variation. The analysis reveals that the SSAMGO algorithm exhibits minimal frequency oscillations and achieves lower SSE compared to other hybrid optimization algorithms. Based on this observation, it can be inferred that the proposed SSAMGO algorithm, which tunes the FOPID and FDVIC parameters, produces a superior and smoother response compared to other tuning methods. Furthermore, it demonstrates minimal undershooting, reduced SSE, and real-time responsiveness under variations in RESs input power.

a: THE SECOND SCENARIO

In this section, the impact of the combination of the proposed FDVIC and DRC technique based on the proposed

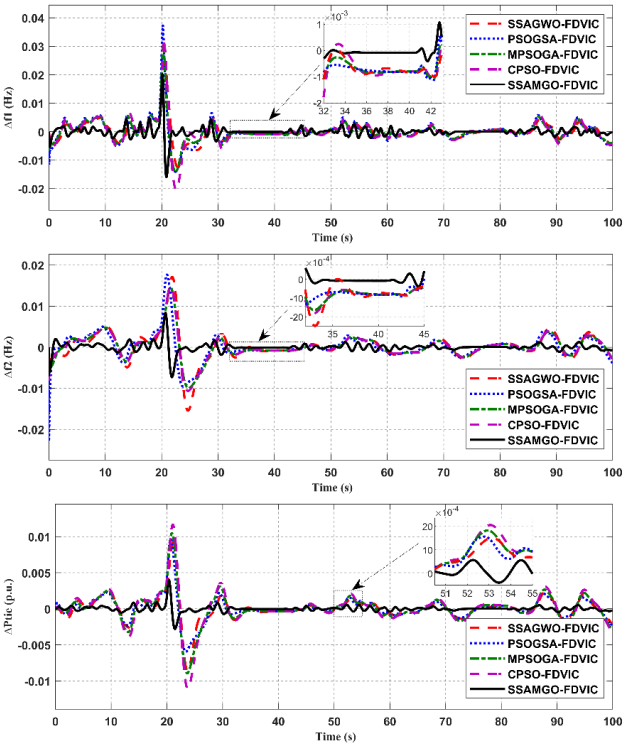

FIGURE 18. Dynamic response of the MMG power system under real-time wind input power.

hybrid SSAMGO on the dynamic performance of MGs is demonstrated and explained.

In order to evaluate the performance of the proposed MMG power system model, the simulation incorporates the combination of the FDVIC techniques from the first scenario with the DRC controller. The responses of this combined system are then simulated and analyzed. In the analysis of the proposed model, it is subjected to sudden changes in load demand. Specifically, a load demand change of 0.12 p.u. is applied to MG1, while MG2 experiences a load demand change of 0.1 p.u. The maximum demand response load available in the analyzed MGs is 0.036 p.u., which corresponds to 30% of the total nominal load of MG1 (240 kW). Similarly, MG2 has a maximum demand response load of 0.025 p.u., which accounts for 25% of its total nominal load (187.5 kW). The value of Toff0 is configured as 10 seconds. Additionally, Δf_{db} is set to -0.05 Hz, and Δf_{prm} is set to -0.55 Hz. In the DR control loop for frequency regulation, 10%, 30%, and 50% of the responsive loads are utilized. The proposed SSAMGO algorithm has been utilized to achieve the optimal value of the DRC parameters. The frequency response of MG1 and MG2, along with the corresponding change in tie line power, is depicted in Fig 19. The findings strongly suggest that the combination of FDVIC and DRC techniques in the examined system offers notable advantages in terms of frequency regulation. The improvements in frequency responses, tie-line power changes, and reduction in frequency

TABLE 8. Frequency deviation and the change in tie line power of MG1 and MG2 of proposed FDVIC combined with DRC techniques.

SSAMGO-FDVIC-DRC	ST (s)	RT (s)	US	OS	SSE	ITAE
			Δf_1			
NO-DRC	4.19	2.5×10^{-7}	-5.25×10^{-3}	1.16×10^{-3}	1.83×10^{-7}	4.19×10^{-3}
10% turn-off of the DR appliance	4.30	1.6×10^{-7}	-4.77×10^{-3}	1.06×10^{-3}	1.07×10^{-7}	3.83×10^{-3}
20% turn-off of the DR appliance	4.43	6.4×10^{-8}	-4.23×10^{-3}	1.01×10^{-3}	3.77×10^{-8}	3.54×10^{-3}
30% turn-off of the DR appliance	4.55	1.1×10^{-5}	-3.69×10^{-3}	0.95×10^{-3}	3.17×10^{-8}	3.65×10^{-3}
40% turn-off of the DR appliance	4.71	3.3×10^{-5}	-3.15×10^{-3}	0.91×10^{-3}	1.01×10^{-7}	3.83×10^{-3}
50% turn-off of the DR appliance	4.92	5.4×10^{-5}	-2.62×10^{-3}	0.86×10^{-3}	1.71×10^{-7}	4.02×10^{-3}
			Δf_2			
NO-DRC	2.17	1.4×10^{-7}	-6.79×10^{-3}	2.13×10^{-3}	1.38×10^{-7}	4.56×10^{-3}
10% turn-off of the DR appliance	2.21	7.7×10^{-8}	-6.04×10^{-3}	1.94×10^{-3}	7.06×10^{-8}	4.08×10^{-3}
20% turn-off of the DR appliance	2.23	1.1×10^{-8}	-5.35×10^{-3}	1.79×10^{-3}	8.56×10^{-9}	3.69×10^{-3}
30% turn-off of the DR appliance	3.54	6.0×10^{-6}	-4.67×10^{-3}	1.64×10^{-3}	5.35×10^{-8}	3.69×10^{-3}
40% turn-off of the DR appliance	3.79	1.5×10^{-5}	-3.99×10^{-3}	1.49×10^{-3}	1.15×10^{-7}	3.75×10^{-3}
50% turn-off of the DR appliance	4.06	2.5×10^{-5}	-3.30×10^{-3}	1.35×10^{-3}	1.77×10^{-7}	3.81×10^{-3}
			ΔP_{tie}			
NO-DRC	4.71	5.5×10^{-4}	-1.45×10^{-4}	2.85×10^{-4}	5.95×10^{-8}	0.75×10^{-3}
10% turn-off of the DR appliance	5.78	3.2×10^{-4}	-1.34×10^{-4}	2.31×10^{-4}	2.94×10^{-8}	0.61×10^{-3}
20% turn-off of the DR appliance	6.19	2.6×10^{-5}	-1.27×10^{-4}	1.92×10^{-4}	2.14×10^{-9}	0.50×10^{-3}
30% turn-off of the DR appliance	6.59	4.67×10^{-5}	-1.19×10^{-4}	1.54×10^{-4}	2.51×10^{-8}	0.59×10^{-3}
40% turn-off of the DR appliance	7.36	1.12×10^{-4}	-1.13×10^{-4}	1.15×10^{-4}	5.24×10^{-8}	0.69×10^{-3}
50% turn-off of the DR appliance	8.03	2.04×10^{-4}	-1.08×10^{-4}	0.78×10^{-4}	7.97×10^{-8}	0.81×10^{-3}

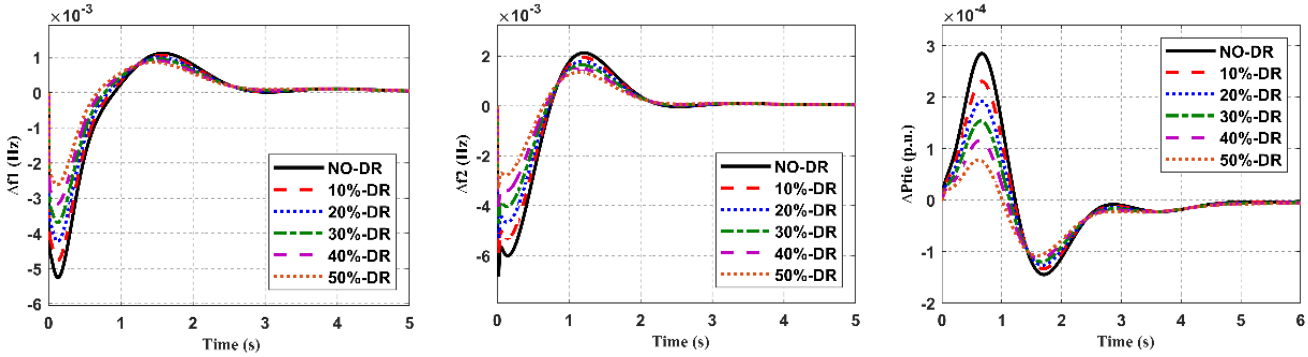

FIGURE 19. Dynamic response of the MG model with a variation of DRC: (a) Frequency deviation of the MG1; (b) Frequency deviation of the MG2; (c) The changing power of the tie line.

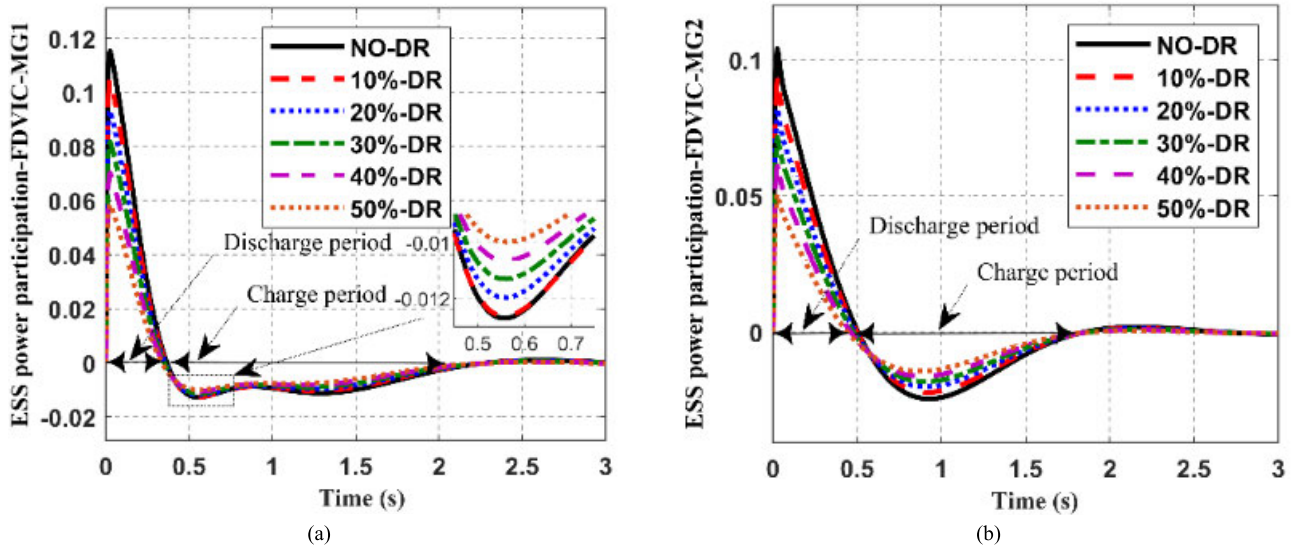

FIGURE 20. Power participation in the ESS of the FDVIC controller loop: (a) ESS of the MG1; (b) ESS of the MG2.

oscillations, as illustrated in Fig. 19 and Table 8, highlight the effectiveness of incorporating DRC units into the system. These results further demonstrate the system's ability to successfully mitigate frequency fluctuations, particularly

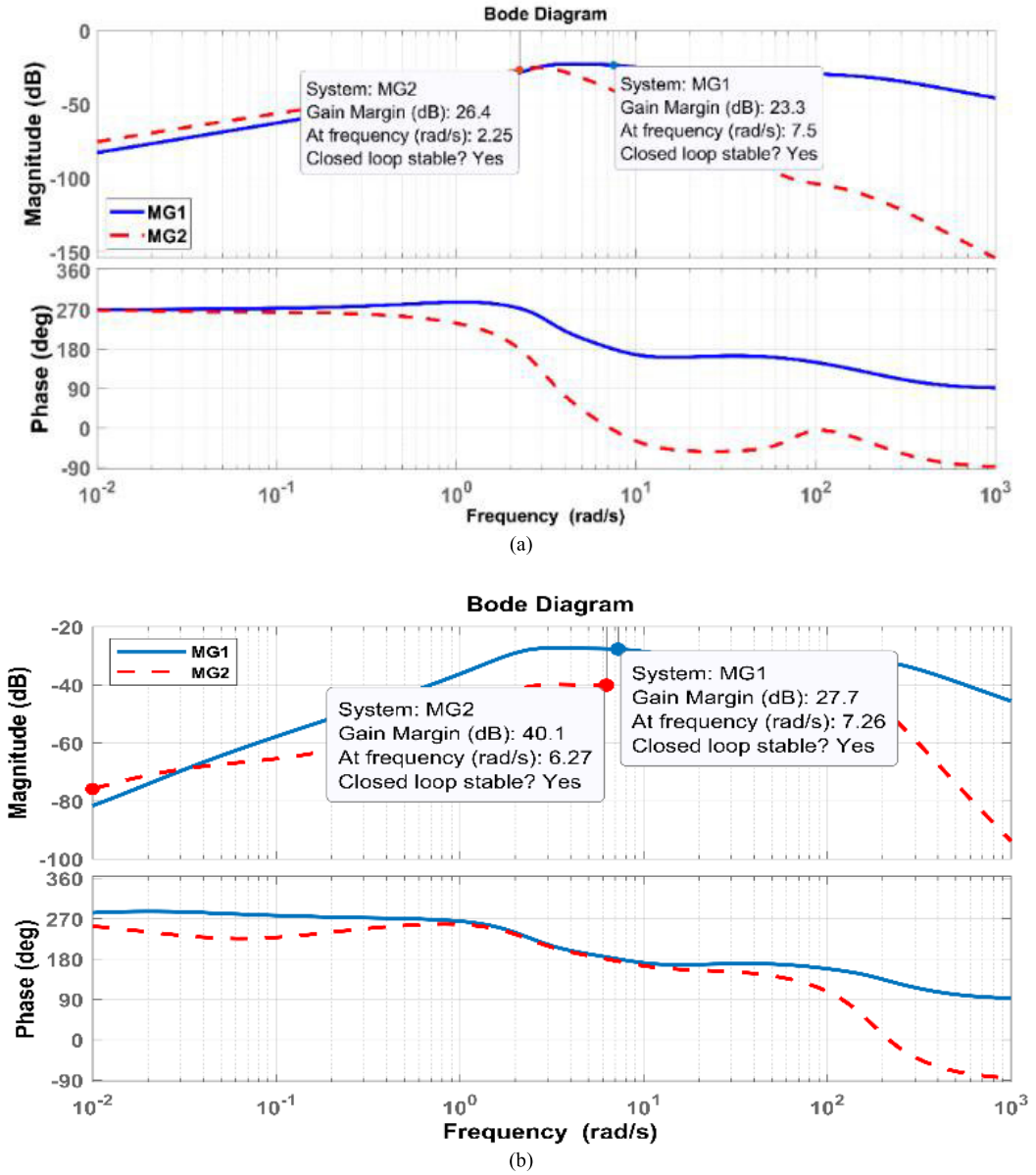

FIGURE 21. Bode analysis of frequency stability: (a) the first scenario, (b) the second scenario.

in scenarios with increased renewable energy penetration, through the integration of demand response support in isolated MGs.

The efficacy of the proposed virtual inertia controller technique is illustrated in Fig. 20, showcasing the effective energy participation from the batteries during the inertia compensation process in the presence of sudden load changes. These results highlight the rapid and efficient charging and discharging of the batteries, validating the effectiveness of the employed method in minimizing frequency deviation and enhancing power system inertia. It is important to note that combining the DRC approach with the FDVIC results in a substantial reduction in active power charging and discharging of the ESS. This reduction significantly improves the lifespan of the ESS, indicating the beneficial impact of the integrated approach.

C. STATE-SPACE MODEL OF MG POWER SYSTEM (STABILITY ANALYSIS)

The system's dynamics are modelled by a set of first-order differential equations that consist of state variables; these are referred to as state equations or a state-space model [51], [52]. The state-space analysis governing the MMG system integrated with RESs presented in Fig. 2 is performed in the absence of the three controllers' actions proposed secondary control loop, virtual inertia control loop, and demand-side response loop. Also, the analysis is shown for the two MG system models, considering the change in load disturbances

in MG1 and MG2. The state space model equations are illustrated in detail in Appendix B.

Fig. 21 depicts the bode-plot diagram of the frequency response for the MMG power system, considering the three controller loop effects in stability analysis. For the first scenario, the gain margin of 23.3 and 26.4 dB and a gain cross-over frequency of 7.5 and 2.25 (rad/s) for MG1 and MG2, respectively. For the second scenario, 27.7 and 40.1 dB of the gain margin and 7.26 and 6.27 (rad/s) of cross-over frequency for MG1 and MG2, respectively. For the proposed SSAMGO-optimized three-loop controller parameters of the MMG power system, the Bode analysis response demonstrates that the closed-loop system is stable.

VI. CONCLUSION

The greater adoption of RESs within MGs has a discernible influence on the stability of the system's frequency. This is primarily attributed to the reduction in the overall system inertia, which subsequently results in significant challenges related to frequency stability. Therefore, a novel approach known as FDVIC is presented, which pertains to a virtual inertia control scheme. This method is designed to improve the dynamic response for the low-inertia MMGs integrated with high penetration of RESs. Furthermore, an adapted DRC has been integrated with the proposed FDVIC technique to mitigate the frequency fluctuations and alleviate the strain on the ESS of the FDVIC during both discharge and charge cycles. The stress on the ESS of the FDVIC for MG1 and MG2 has seen a decrease of 49.15% and 51.37%, respectively, during the discharging period. Furthermore, the power necessary to charge the ESS of the FDVIC has been reduced by 21.34% for MG1 and 41.47% for MG2. Additionally, FOPID controllers have been implemented to govern the active power output of both the biodiesel generators and the Geothermal station of the proposed MG. The optimal parameters for the three-loop controller were determined through the utilization of the SSAMGO algorithm. An extensive assessment of SSAMGO's performance was conducted, comparing it to various other optimization algorithms in different scenarios. The controllers' robustness was further confirmed through testing under concurrent alterations in wind power, solar PV irradiation, and load fluctuations. The proposed controllers notably minimized both the OS, US, ST, RT, and SSE of frequency and tie-line power deviations. The stability analysis of two scenarios, conducted through Bode analysis, demonstrates that the calibrated gain values for the three-loop controllers are apt for maintaining the system's stable operation. The simulation results clearly show that the FDVIC technique proposed in this study provides adequate inertia to maintain MG stability. The future directions of this research can be succinctly encapsulated as the application of the proposed controller to uphold the stability of an MMG system operating in grid-connected mode, with a specific focus on real-time applications.

APPENDIXES

APPENDIX A

The parameters of the proposed multi-MG integrated with RESs:

MG rated power: $P_{r1} = 2000$ kW, $P_{r2} = 1500$ kW; Power system gains constant: $k_{p1} = 125$ Hz/p.u.MW, $k_{p2} = 100$ Hz/p.u.MW; Power system time constant: $T_{p1} = 25$ s, $T_{p2} = 12$ s; Frequency bias factor: $B_1 = B_2 = 0.4267$ p.u.MW/Hz; Damping coefficient: $D_1 = 0.00833$ p.u.MW/Hz, $D_2 = 0.01$ p.u.MW/Hz; Droop control: $R_1 = R_2 = 2.4$ Hz/p.u.MW; Equivalent system inertia: $H_{eq.1} = 3.5106$ s, $H_{eq.2} = 0.75$ s; Tie-line power flow time constants: $T_{12} = T_{21} = 0.08674$ p.u.MW/rad; Biodiesel valve gain: $K_{VA1} = K_{VA2} = 1$; Biodiesel valve actuator delay: $T_{VA1} = T_{VA2} = 0.05$ s; Biodiesel engine gain: $K_{BE1} = K_{BE2} = 1$; Time constants of biodiesel: $T_{BE1} = T_{BE2} = 0.5$ s; Gain constant of WT: $K_{WT1} = K_{WT2} = 1$; Time constant of WT: $T_{WT1} = T_{WT2} = 1.5$ s; Gain constant of PV: $K_{PV1} = K_{PV2} = 1$; Time constant of PV: $T_{PV1} = T_{PV2} = 1.8$ s; Gain of the turbine of solar thermal: $K_T = 1$; Charging time constant of the turbine of solar thermal: $T_T = 0.3$ s; Solar collector gain: $K_S = 1.8$; Solar collector time constant: $T_S = 1.8$ s; Gain constant of the ESS: $K_{BESS1} = K_{BESS2} = 1$; Time constant of the ESS: $T_{BESS1} = T_{BESS2} = 0.026$ s.

APPENDIX B

The state-space model of the proposed MG model is given as:

$$X^{\bullet} = AX + B_1W + B_2u \tag{33}$$

$$Y = CX \tag{34}$$

where A matrix is represented as:

$$A = \begin{bmatrix} a_{11} & a_{12} & a_{13} & \dots & a_{120} \\ a_{21} & a_{22} & a_{23} & \dots & a_{220} \\ a_{31} & a_{32} & a_{33} & \dots & a_{320} \\ \cdot & \cdot & \cdot & \dots & \cdot \\ a_{201} & a_{202} & a_{203} & \dots & a_{2020} \end{bmatrix} \tag{35}$$

The model will include a total of 20 modelled state variables, and its vector form is as follows:

$$X = [X_1, X_2, X_3, \dots\dots\dots\dots, X_{20}]^T \tag{36}$$

The state variables that relate to the system parameters are denoted as:

$$\begin{aligned} X = \big[&\Delta f_1, \Delta P_{BDG}, \Delta P_{vl}, \Delta P_{FO1}, \Delta P_{Geo}, \Delta P_{gl}, \Delta P_{STH}, \\ &\Delta P_T, \Delta P_{WTG1}, \Delta P_{inertial}, \Delta P_{DRC1}, \Delta P_{tiej}, \Delta f_2, \Delta P_{BDG2}, \\ &\Delta P_{v2}, \Delta P_{FO2}, \Delta P_{WGG2}, \Delta P_{FV}, \Delta P_{ineri\,2}, \Delta P_{DRC2}\big]^T \end{aligned} \tag{37}$$

Following is a description of the state-space equations of the proposed model:

$$\begin{aligned} X_1^{\bullet} = [&a_{11}X_1 + a_{12}X_2 + a_{15}X_5 + a_{17}X_7 + a_{19}X_9 \pm a_{110}X_{10} \\ &\pm a_{111}X_{11} - \Delta P_{loall}\,] \end{aligned} \tag{38}$$

where $a_{1\,1} = \frac{-D_1}{2H_1}$, $a_{1\,2} = a_{1\,5} = a_{1\,7} = a_{1\,9} = a_{1\,10} = a_{1\,11} = \frac{K_{ps1}}{2H_1}$

The biodiesel generator state-space model of MG1 is as follows:

$$X_2^{\bullet} = a_{22}X_2 + a_{23}X_3 = \frac{-1}{T_{BEI}}X_2 + \frac{K_{BE1}}{T_{BE1}}X_3 \tag{39}$$

$$X_3^{\bullet} = a_{31}X_1 + a_{33}X_3 + a_{34}X_4 = \frac{-K_{VA1}}{R_1T_{VA1}}X_1 - \frac{1}{T_{VAl}}X_3 + \frac{K_{VA1}}{T_{VAl}}X_4 \tag{40}$$

The geothermal generator state-space model is depicted as follows:

$$X_5^{\bullet} = a_{55}X_5 + a_{56}X_6 = \frac{-1}{T_{tg}}X_5 + \frac{K_{tg}}{T_{tg}}X_6 \tag{41}$$

$$X_6^{\bullet} = a_{64}X_4 + a_{66}X_6 = \frac{K_{g8}}{T_{gg}}X_4 - \frac{1}{T_{gg}}X_6 \tag{42}$$

The state-space model of the solar thermal power generator is as follows:

$$X_7^{\bullet} = a_{77}X_7 + a_{78}X_8 = \frac{-1}{T_5}X_7 + \frac{K_8}{T_8}X_8 \tag{43}$$

$$X_8^{\bullet}a_{88}X_8 + \frac{K_T}{T_T}P_{solur\text{-}themal} = \frac{-1}{T_T}X_8 + \frac{K_T}{T_T}P_{solur\text{-}themal} \tag{44}$$

The state-space model of the wind-turbine generator of MG1 is as follows:

$$X_9^{\bullet} = a_{99}X_9 + \frac{K_{WTGl}}{T_{WTGl}}P_{xind} = \frac{-1}{T_{WTGl}}X_9 + \frac{K_{WTGl}}{T_{WTGl}}P_{rind} \tag{45}$$

The state-space of the proposed FDVIC controller based on ESS in the MG1 is as follows:

$$X_{10}^{\bullet} = a_{101}X_1 \cdot \Delta P_{FDVCl} + a_{1010}X_{10} = \frac{K_{ESS}}{T_{ESS}}X_1 \cdot \Delta P_{FDVCl} - \frac{1}{T_{ESS}}X_{10} \tag{46}$$

The tie-lines of the interconnected MGs system are portrayed as follows:

$$X_{12}^{\bullet} = \Delta P_{ta,i} = 2\pi\left[\sum_{i=i,i\neq j}^{n} T_{ij}X_i\right] \tag{47}$$

The state-space of the frequency deviation of MG2 is as follows:

$$X_{13}^{\bullet} = [a_{1313}X_{13} + a_{1314}X_{14} + a_{1317}X_{17} + a_{1318}X_{18} \pm a_{1319}X_{19} \pm a_{1320}X_{20} - \Delta P_{load\,2}] \tag{48}$$

where $a_{13\,13} = \frac{-D_2}{2H_2}$, $a_{13\,14} = a_{13\,17} = a_{13\,18} = a_{13\,19} = a_{13\,20} = \frac{K_{ps2}}{2H_2}$

The biodiesel generator state-space model of MG2 is as follows:

$$X_{14}^{\bullet} = a_{1414}X_{14} + a_{1415}X_{15} = \frac{-1}{T_{BE2}}X_{14} + \frac{K_{BE2}}{T_{BE2}}X_{15} \tag{49}$$

$$X_{15}^{\bullet} = a_{1513}X_{13} + a_{1515}X_{15} + a_{15}X_{16} = \frac{-K_{VA2}}{R_2T_{VA2}}X_{13} - \frac{1}{T_{VA2}}X_{15} + \frac{K_{VA2}}{T_{VA2}}X_{16} \tag{50}$$

The state-space model of the wind-turbine generator of MG2 is as follows:

$$X_{17}^{\bullet} = a_{1717}X_{17} + \frac{K_{WTG2}}{T_{WTG2}}P_{wind} = \frac{-1}{T_{WTG2}}X_{17} + \frac{K_{WTG2}}{T_{WTG2}}P_{wind} \tag{51}$$

The state-space model of the solar photovoltaic RES is as follows:

$$X_{18}^{\bullet} = a_{18\,18}X_{18} + \frac{K_{pV}}{T_{pV}}P_{solar} = \frac{-1}{T_{pV}}X_{18} + \frac{K_{pV}}{T_{pV}}P_{solar} \tag{52}$$

The state-space of the proposed FDVIC controller based on ESS in the MG2 is as follows:

$$X_{19}^{\bullet} = a_{191}X_{13} \cdot \Delta P_{FDVC2} + a_{1919}X_{19} = \frac{K_{ESS}}{T_{ESS}}X_{13} \cdot \Delta P_{FDVC2} - \frac{1}{T_{ESS}}X_{19} \tag{53}$$

MG disturbance signals considered in this research article include the change in wind power (P_{wind}), solar radiation power (P_{solar}), solar thermal power ($P_{solar-thermal}$), and load power (P_{load}):

$$W = [\Delta P_{wixd}\,,\ \Delta P_{solar}\,,\ \Delta P_{solar\text{-}themal}\,,\ \Delta P_{load}\,]^T \tag{54}$$

The control signals of the MMG model are as follows:

$$u = [\Delta P_{FO1}, \Delta P_{FO2}, \Delta P_{inetria1}\,, \Delta P_{inertia\,2}, \Delta P_{DRC1}, \Delta P_{DRC2}]^T \tag{55}$$

The output matrix model of the MG is defined as:

$$Y = [\Delta f_1, \Delta P_{BDG1}, \Delta P_{Ge0}, \Delta P_{STH}, \Delta P_{WTG1}, \Delta P_{inertial}\,, \Delta P_{DRC1}, \Delta f_2, \Delta P_{BDG2}, \Delta P_{WTG2}, \Delta P_{PV}, \Delta P_{inertia\,2}, \Delta P_{DRC2}]^T \tag{56}$$

$$\therefore Y = \begin{bmatrix}1 & 0 & 0 & 0 & 0 & 1 & 0 & 0 & 0 & 0\end{bmatrix}^T \cdot [X]^T \tag{57}$$

The above state-space modelling is derived for the low inertia MMG system integrated with RESs. The operation of the biodiesel generators with the RESs during the study of the first scenario and second scenario control technique resulted in 20 state variables, and this will lead to the order of the closed loop transfer function being powered to 35.

The proposed model shown in Fig. 2 can be simplified as shown in Fig. 22 to illustrate the closed-loop control technique used in this study.

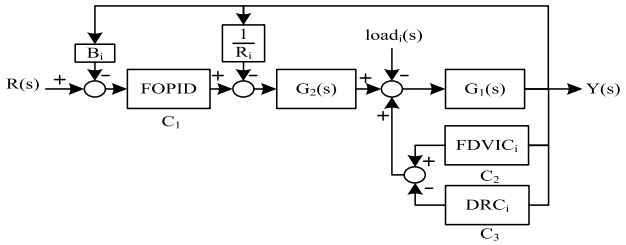

FIGURE 22. Closed loop control of the proposed MG.

The total response of the interconnected MGs system was modelled with three controller loops (C1, C2, and C3) as the following:

$$\begin{aligned} &R(s)C_1G_1(s)G_2(s) - B_iY(s)C_1G_1(s)G_2(s) \\ &\quad - \frac{1}{R_i}Y(s)G_1(s) \\ &G_2(s) - D_i(s)G_1(s) + Y(s)C_2G_1(s) - Y(s)C_3G_1(s) \\ &\quad = Y(s) \end{aligned} \tag{58}$$

$$\therefore Y(s) = Y_{11}(s) + Y_{12}(s) \tag{59}$$

where

$$Y_{11}(s) = \frac{R(s)C_1G_1(s)G_2(s)}{B_iC_1G_1(s)G_2(s)+\frac{1}{R_i}G_1(s)G_2(s) - C_2G_1(s)+C_3G_1(s)} \tag{60}$$

and

$$Y_{12}(s) = \frac{-D_i(s)G_1(s)}{B_iC_1G_1(s)G_2(s)+\frac{1}{R_i}G_1(s)G_2(s) - C_2G_1(s)+C_3G_1(s)} \tag{61}$$

The closed-loop transfer function of the proposed model shown in Fig. 22 is used to address the change in the load demand and the variation in tie-line power in (62) and (63), respectively.

$$\Delta f|_{\Delta P_{load}} = \frac{-G_1}{1 + G_1\left[B_iC_1G_2 + \frac{1}{R_i}G_2 - C_2 + C_3\right]}\Delta P_{load} \tag{62}$$

$$\Delta f|_{\Delta P_{ie}} = \frac{C_1G_1G_2}{1 + G_1\left[B_iC_1G_2 + \frac{1}{R_i}G_2 - C_2 + C_3\right]}\Delta P_{tie} \tag{63}$$

By applying the superposition theorem, the closed-loop transfer function for the total variations of the frequency response of the proposed MG can be represented as follows:

$$\Delta f = \frac{-G_1\Delta P_{load} + C_1G_1G_2\Delta P_{tie}}{1 + G_1\left[B_iC_1G_2 + \frac{1}{R_i}G_2 - C_2 + C_3\right]} \tag{64}$$

ACKNOWLEDGMENT

The authors would like to thank the reviewers for their constructive comments to improve the quality of the manuscript.

REFERENCES

[1] A. X. R. Irudayaraj, N. I. A. Wahab, V. Veerasamy, M. Premkumar, M. A. M. Radzi, N. B. Sulaiman, and W.-S. Tan, "Distributed intelligence for consensus-based frequency control of multi-microgrid network with energy storage system," *J. Energy Storage*, vol. 73, Dec. 2023, Art. no. 109183, doi: 10.1016/j.est.2023.109183.

[2] N. K. Roy, S. Islam, A. K. Podder, T. K. Roy, and S. M. Muyeen, "Virtual inertia support in power systems for high penetration of renewables—Overview of categorization, comparison, and evaluation of control techniques," *IEEE Access*, vol. 10, pp. 129190–129216, 2022, doi: 10.1109/ACCESS.2022.3228204.

[3] R. Sowmya, M. Premkumar, C. Kumar, and A. X. R. Irudayaraj, "Frequency regulation in multi-microgrid power system using an adaptive Beluga whale optimizer-based FOPID controller," in *Proc. IEEE 3rd Int. Conf. Sustain. Energy Future Electric Transp. (SEFET)*, Bhubaneswar, India, Aug. 2023, pp. 1–6, doi: 10.1109/sefet57834.2023.10245312.

[4] N. Sockeel, J. Gafford, B. Papari, and M. Mazzola, "Virtual inertia emulator-based model predictive control for grid frequency regulation considering high penetration of inverter-based energy storage system," *IEEE Trans. Sustain. Energy*, vol. 11, no. 4, pp. 2932–2939, Oct. 2020, doi: 10.1109/TSTE.2020.2982348.

[5] M. H. Khooban, "An optimal non-integer model predictive virtual inertia control in inverter-based modern AC power grids-based V2G technology," *IEEE Trans. Energy Convers.*, vol. 36, no. 2, pp. 1336–1346, Jun. 2021, doi: 10.1109/TEC.2020.3030655.

[6] P. Saxena, N. Singh, and A. K. Pandey, "Self-regulated solar PV systems: Replacing battery via virtual inertia reserve," *IEEE Trans. Energy Convers.*, vol. 36, no. 3, pp. 2185–2194, Sep. 2021, doi: 10.1109/TEC.2021.3052022.

[7] S. Oshnoei, M. Aghamohammadi, S. Oshnoei, A. Oshnoei, and B. Mohammadi-Ivatloo, "Provision of frequency stability of an islanded microgrid using a novel virtual inertia control and a fractional order cascade controller," *Energies*, vol. 14, no. 14, p. 4152, Jul. 2021, doi: 10.3390/en14144152.

[8] M. Nour, G. Magdy, A. Bakeer, A. A. Telba, A. Beroual, U. Khaled, and H. Ali, "A new fractional-order virtual inertia support based on battery energy storage for enhancing microgrid frequency stability," *Fractal Fractional*, vol. 7, no. 12, p. 855, Nov. 2023, doi: 10.3390/fractalfract7120855.

[9] A. K. Barik and D. C. Das, "Proficient load-frequency regulation of demand response supported bio-renewable cogeneration based hybrid microgrids with quasi-oppositional selfish-herd optimisation," *IET Gener., Transmiss. Distrib.*, vol. 13, no. 13, pp. 2889–2898, Jul. 2019, doi: 10.1049/iet-gtd.2019.0166.

[10] S. A. Hosseini, M. Toulabi, A. Ashouri-Zadeh, and A. M. Ranjbar, "Battery energy storage systems and demand response applied to power system frequency control," *Int. J. Electr. Power Energy Syst.*, vol. 136, Mar. 2022, Art. no. 107680, doi: 10.1016/j.ijepes.2021.107680.

[11] T. Kerdphol, Y. Qudaih, and Y. Mitani, "Optimum battery energy storage system using PSO considering dynamic demand response for microgrids," *Int. J. Electr. Power Energy Syst.*, vol. 83, pp. 58–66, Dec. 2016, doi: 10.1016/j.ijepes.2016.03.064.

[12] A. Al-Hinai, H. Alyammahi, and H. H. Alhelou, "Coordinated intelligent frequency control incorporating battery energy storage system, minimum variable contribution of demand response, and variable load damping coefficient in isolated power systems," *Energy Rep.*, vol. 7, pp. 8030–8041, Nov. 2021, doi: 10.1016/j.egyr.2021.07.072.

[13] S. Mohammed, Y. A. Sha'aban, I. J. Umoh, A. T. Salawudeen, and S. M. Ibn Shamsah, "A hybrid smell agent symbiosis organism search algorithm for optimal control of microgrid operations," *PLoS ONE*, vol. 18, no. 6, Jun. 2023, Art. no. e0286695, doi: 10.1371/journal.pone.0286695.

[14] M. A. Nezhad and H. Bevrani, "Frequency control in an islanded hybrid microgrid using frequency response analysis tools," *IET Renew. Power Gener.*, vol. 12, no. 2, pp. 227–243, Feb. 2018, doi: 10.1049/iet-rpg.2017.0227.

[15] K. Sabahi, M. Tavan, and A. Hajizadeh, "Adaptive type-2 fuzzy PID controller for LFC in AC microgrid," *Soft Comput.*, vol. 25, no. 11, pp. 7423–7434, Jun. 2021, doi: 10.1007/s00500-021-05704-6.

[16] M. Joshi, G. Sharma, and E. Çelik, "Load frequency control of hydro-hydro power system using Fuzzy-PSO-PID with application of UC and RFB," *Electr. Power Compon. Syst.*, vol. 51, no. 12, pp. 1156–1170, Jul. 2023, doi: 10.1080/15325008.2023.2196663.

[17] M. Joshi, G. Sharma, P. N. Bokoro, and N. Krishnan, "A Fuzzy-PSO-PID with UPFC-RFB solution for an LFC of an interlinked hydro power system," *Energies*, vol. 15, no. 13, p. 4847, Jul. 2022, doi: 10.3390/en15134847.

[18] B. Yildirim, P. Razmi, A. Fathollahi, M. Gheisarnejad, and M. H. Khooban, "Neuromorphic deep learning frequency regulation in stand-alone microgrids," *Appl. Soft Comput.*, vol. 144, Sep. 2023, Art. no. 110418, doi: 10.1016/j.asoc.2023.110418.

[19] R. K. Rojin and M. Mary Linda, "Hybrid microgrid based on PID controller with the modified particle swarm optimization," *Intell. Autom. Soft Comput.*, vol. 33, no. 1, pp. 245–258, 2022, doi: 10.32604/iasc.2022.021834.

[20] L. Zhang, H. Zheng, G. Cai, Z. Zhang, X. Wang, and L. H. Koh, "Power-frequency oscillation suppression algorithm for AC microgrid with multiple virtual synchronous generators based on fuzzy inference system," *IET Renew. Power Gener.*, vol. 16, no. 8, pp. 1589–1601, Jun. 2022, doi: 10.1049/rpg2.12461.

[21] M. A. Sobhy, H. M. Hasanien, A. Y. Abdelaziz, and M. Ezzat, "Manta ray foraging optimization algorithm-based load frequency control for hybrid modern power systems," *IET Renew. Power Gener.*, vol. 17, no. 6, pp. 1466–1487, Apr. 2023, doi: 10.1049/rpg2.12688.

[22] A. Tepljakov, B. B. Alagoz, C. Yeroglu, E. A. Gonzalez, S. H. Hosseinnia, E. Petlenkov, A. Ates, and M. Cech, "Towards industrialization of FOPID controllers: A survey on milestones of fractional-order control and pathways for future developments," *IEEE Access*, vol. 9, pp. 21016–21042, 2021, doi: 10.1109/ACCESS.2021.3055117.

[23] A. Fathy and A. G. Alharbi, "Recent approach based movable damped wave algorithm for designing fractional-order PID load frequency control installed in multi-interconnected plants with renewable energy," *IEEE Access*, vol. 9, pp. 71072–71089, 2021, doi: 10.1109/ACCESS.2021.3078825.

[24] D. Guha, P. K. Roy, S. Banerjee, S. Padmanaban, F. Blaabjerg, and D. Chittathuru, "Small-signal stability analysis of hybrid power system with quasi-oppositional sine cosine algorithm optimized fractional order PID controller," *IEEE Access*, vol. 8, pp. 155971–155986, 2020, doi: 10.1109/ACCESS.2020.3018620.

[25] Y. L. Karnavas and E. Nivolianiti, "Optimal load frequency control of a hybrid electric shipboard microgrid using jellyfish search optimization algorithm," *Appl. Sci.*, vol. 13, no. 10, p. 6128, May 2023, doi: 10.3390/app13106128.

[26] M. D., J. K., P. Shah, and R. Sekhar, "Fractional order PIλDμ controller for microgrid power system using cohort intelligence optimization," *Results Control Optim.*, vol. 11, Jun. 2023, Art. no. 100218, doi: 10.1016/j.rico.2023.100218.

[27] N. Sundararaju, A. Vinayagam, V. Veerasamy, and G. Subramaniam, "A chaotic search-based hybrid optimization technique for automatic load frequency control of a renewable energy integrated power system," *Sustainability*, vol. 14, no. 9, p. 5668, May 2022, doi: 10.3390/su14095668.

[28] N. Paliwal, L. Srivastava, and M. Pandit, "Application of grey wolf optimization algorithm for load frequency control in multi-source single area power system," *Evol. Intell.*, vol. 15, no. 1, pp. 563–584, Mar. 2022, doi: 10.1007/s12065-020-00530-5.

[29] M. H. M. Ashnani, A. Johari, H. Hashim, and E. Hasani, "A source of renewable energy in Malaysia, why biodiesel?" *Renew. Sustain. Energy Rev.*, vol. 35, pp. 244–257, Jul. 2014, doi: 10.1016/j.rser.2014.04.001.

[30] A. Rafiee, Y. Batmani, F. Ahmadi, and H. Bevrani, "Robust load-frequency control in islanded microgrids: Virtual synchronous generator concept and quantitative feedback theory," *IEEE Trans. Power Syst.*, vol. 36, no. 6, pp. 5408–5416, Nov. 2021, doi: 10.1109/TPWRS.2021.3077768.

[31] A. K. Barik and D. C. Das, "Expeditious frequency control of solar photovoltaic/biogas/biodiesel generator based isolated renewable microgrid using grasshopper optimisation algorithm," *IET Renew. Power Gener.*, vol. 12, no. 14, pp. 1659–1667, Oct. 2018, doi: 10.1049/iet-rpg.2018.5196.

[32] A. X. R. Irudayaraj, N. I. A. Wahab, V. Veerasamy, M. Premkumar, M. A. M. Radzi, N. B. Sulaiman, and H. Haes Alhelou, "Decentralized frequency control of restructured energy system using hybrid intelligent algorithm and non-linear fractional order proportional integral derivative controller," *IET Renew. Power Gener.*, vol. 17, no. 8, pp. 2009–2037, Jun. 2023, doi: 10.1049/rpg2.12746.

[33] S. Mekhilef, A. Safari, W. E. S. Mustaffa, R. Saidur, R. Omar, and M. A. A. Younis, "Solar energy in Malaysia: Current state and prospects," *Renew. Sustain. Energy Rev.*, vol. 16, no. 1, pp. 386–396, Jan. 2012, doi: 10.1016/j.rser.2011.08.003.

[34] G. Shankar and V. Mukherjee, "Load frequency control of an autonomous hybrid power system by quasi-oppositional harmony search algorithm," *Int. J. Electr. Power Energy Syst.*, vol. 78, pp. 715–734, Jun. 2016, doi: 10.1016/j.ijepes.2015.11.091.

[35] B. A. Fadheel, N. I. A. Wahab, A. J. Mahdi, M. Premkumar, M. A. B. M. Radzi, A. B. C. Soh, V. Veerasamy, and A. X. R. Irudayaraj, "A hybrid grey wolf assisted-sparrow search algorithm for frequency control of RE integrated system," *Energies*, vol. 16, no. 3, p. 1177, Jan. 2023, doi: 10.3390/en16031177.

[36] M. Tavakoli, E. Pouresmaeil, J. Adabi, R. Godina, and J. P. S. Catalão, "Load-frequency control in a multi-source power system connected to wind farms through multi terminal HVDC systems," *Comput. Oper. Res.*, vol. 96, pp. 305–315, Aug. 2018, doi: 10.1016/j.cor.2018.03.002.

[37] H. H. Fayek and P. Kotsampopoulos, "Central tunicate swarm NFOPID-based load frequency control of the Egyptian power system considering new uncontrolled wind and photovoltaic farms," *Energies*, vol. 14, no. 12, p. 3604, Jun. 2021, doi: 10.3390/en14123604.

[38] K. S. El-Bidairi, H. D. Nguyen, T. S. Mahmoud, S. D. G. Jayasinghe, and J. M. Guerrero, "Optimal sizing of battery energy storage systems for dynamic frequency control in an islanded microgrid: A case study of flinders island, Australia," *Energy*, vol. 195, Mar. 2020, Art. no. 117059, doi: 10.1016/j.energy.2020.117059.

[39] H. Shayeghi, A. Rahnama, and H. H. Alhelou, "Frequency control of fully-renewable interconnected microgrid using fuzzy cascade controller with demand response program considering," *Energy Rep.*, vol. 7, pp. 6077–6094, Nov. 2021, doi: 10.1016/j.egyr.2021.09.027.

[40] Y. Bao, Y. Li, Y. Hong, and B. Wang, "Design of a hybrid hierarchical demand response control scheme for the frequency control," *IET Gener., Transmiss. Distrib.*, vol. 9, no. 15, pp. 2303–2310, Nov. 2015, doi: 10.1049/iet-gtd.2015.0628.

[41] M. S. Uz Zaman, S. Bukhari, K. Hazazi, Z. Haider, R. Haider, and C.-H. Kim, "Frequency response analysis of a single-area power system with a modified LFC model considering demand response and virtual inertia," *Energies*, vol. 11, no. 4, p. 787, Mar. 2018, doi: 10.3390/en11040787.

[42] A. X. R. Irudayaraj, N. I. A. Wahab, M. Premkumar, M. A. M. Radzi, N. B. Sulaiman, V. Veerasamy, R. A. Farade, and M. Z. Islam, "Renewable sources-based automatic load frequency control of interconnected systems using chaotic atom search optimization," *Appl. Soft Comput.*, vol. 119, Apr. 2022, Art. no. 108574, doi: 10.1016/j.asoc.2022.108574.

[43] A. Tabak and S. Duman, "Maiden application of TIDμ1NDμ2 controller for effective load frequency control of non-linear two-area power system," *IET Renew. Power Gener.*, pp. 1–23, Aug. 2023, doi: 10.1049/rpg2.12817.

[44] J. Xue and B. Shen, "A novel swarm intelligence optimization approach: Sparrow search algorithm," *Syst. Sci. Control Eng.*, vol. 8, no. 1, pp. 22–34, Jan. 2020, doi: 10.1080/21642583.2019.1708830.

[45] B. Abdollahzadeh, F. S. Gharehchopogh, N. Khodadadi, and S. Mirjalili, "Mountain gazelle optimizer: A new nature-inspired metaheuristic algorithm for global optimization problems," *Adv. Eng. Softw.*, vol. 174, Dec. 2022, Art. no. 103282, doi: 10.1016/j.advengsoft.2022.103282.

[46] R. Abbassi, S. Saidi, S. Urooj, B. N. Alhasnawi, M. A. Alawad, and M. Premkumar, "An accurate metaheuristic mountain gazelle optimizer for parameter estimation of single- and double-diode photovoltaic cell models," *Mathematics*, vol. 11, no. 22, p. 4565, Nov. 2023, doi: 10.3390/math11224565.

[47] J. K. Kailasam, R. Nalliah, S. N. Muthusamy, and P. Manoharan, "MLBRSA: Multi-learning-based reptile search algorithm for global optimization and software requirement prioritization problems," *Biomimetics*, vol. 8, no. 8, p. 615, 2023, doi: 10.3390/biomimetics8080615.

[48] R. Sowmya, M. Premkumar, and P. Jangir, "Newton-Raphson-based optimizer: A new population-based metaheuristic algorithm for continuous optimization problems," *Eng. Appl. Artif. Intell.*, vol. 128, Feb. 2024, Art. no. 107532, doi: 10.1016/j.engappai.2023.107532.

[49] C. S. S. Ganesh, C. Kumar, M. Premkumar, and B. Derebew, "Enhancing photovoltaic parameter estimation: Integration of non-linear hunting and reinforcement learning strategies with golden jackal optimizer," *Sci. Rep.*, vol. 14, no. 1, p. 2756, Feb. 2024, doi: 10.1038/s41598-024-52670-8.

[50] A. A. Kadhem, N. I. A. Wahab, and A. N. Abdalla, "Wind energy generation assessment at specific sites in a peninsula in Malaysia based on reliability indices," *Processes*, vol. 7, no. 7, p. 399, Jun. 2019, doi: 10.3390/pr7070399.
[51] V. Veerasamy, N. I. A. Wahab, R. Ramachandran, M. L. Othman, H. Hizam, A. X. R. Irudayaraj, J. M. Guerrero, and J. S. Kumar, "A Hankel matrix based reduced order model for stability analysis of hybrid power system using PSO-GSA optimized cascade PI-PD controller for automatic load frequency control," *IEEE Access*, vol. 8, pp. 71422–71446, 2020, doi: 10.1109/ACCESS.2020.2987387.
[52] H. H. Alhelou, N. Nagpal, N. Kassarwani, and P. Siano, "Decentralized optimized integral sliding mode-based load frequency control for interconnected multi-area power systems," *IEEE Access*, vol. 11, pp. 32296–32307, 2023, doi: 10.1109/ACCESS.2023.3262790.

BASHAR ABBAS FADHEEL received the B.E. degree in electrical and engineering (power and machine) and the M.Sc. degree in power electronics from the University of Mosul, Mosul, Iraq, in 2002 and 2011, respectively. He is currently pursuing the Ph.D. degree in electrical power engineering with Universiti Putra Malaysia, Seri Kembangan, Malaysia. Since 2020, he has been a Lecturer with the Faculty of Engineering, University of Kerbala, Karbala, Iraq. His research interests include the design of robust controllers for power system applications, power system stability, microgrid systems, and renewable energy resources.

NOOR IZZRI ABDUL WAHAB (Senior Member, IEEE) received the degree in electrical and electronic engineering from the University of Manchester Institute of Science and Technology (UMIST), U.K., in 1998, the M.Sc. degree in electrical power engineering from Universiti Putra Malaysia (UPM), in 2002, and the Ph.D. degree in electrical, electronic and system engineering from Universiti Kebangsaan Malaysia (UKM), in 2010. He is currently an Associate Professor with the Department of Electrical and Electronic Engineering, Faculty of Engineering, UPM, where he is also the Founding Member of the Advanced Lightning, Power and Energy Research Centre (ALPER). His research interests include power system stability, application of AI in power systems, and power quality. He is a registered Chartered Engineer (C.Eng.), a Professional Engineer (Ir.), and a member of the Institution of Engineers Malaysia (IEM).

PREMKUMAR MANOHARAN (Senior Member, IEEE) was born in Coimbatore, India. He received the B.E. degree in electrical and electronics engineering from the Sri Ramakrishna Institute of Technology, Coimbatore, in 2004, the M.E. degree in applied electronics from the Anna University of Technology, Coimbatore, in 2010, and the Ph.D. degree from Anna University, Chennai, India, in 2019. He is currently an Associate Professor and the Head with the Dayananda Sagar College of Engineering, Bengaluru, India. Also, he is a Research Fellow with the Institute of Power Engineering, Universiti Tenaga Nasional (UNITEN), Kajang, Malaysia. He has over 15 years of teaching experience. He has published over 140 technical articles in various national/international peer-reviewed journals, such as IEEE, Elsevier, and Springer, with over 2900 citations and an H-index of 31. He has published/granted seven patents by IPR, India; and IPR, Australia. According to the report published by Stanford University in 2021, 2022, and 2023, he was one of the 2% influential scholars, which depicts the 100,000 top scientists in the world. His current research interests include optimization algorithms, including single-, multi-, and many-objectives for different real-world engineering design problems, power converters/inverters, PV parameter extraction, PV MPPT, PV array faults, smart grids and microgrids, frequency regulation, BMS for electric vehicles, and non-isolated/isolated dc–dc converters for renewable energy systems and EVs. He is a member of various professional bodies, such as ISTE and IAENG. He is also an editor/a reviewer of leading journals of different publishers, such as IEEE, IET, Wiley, Taylor & Francis, Springer, and MDPI.

ALI JAFER MAHDI received the B.Sc. and M.Sc. degrees in electrical power and machines from the University of Technology, Iraq, in 1995 and 1997, respectively, and the Ph.D. degree from the University of Liverpool, U.K., in 2011. He is a Distinguished Electrical Engineering Professor. Currently, he is the Director of the Scientific Affairs Department, Al-Zahraa University for Women. Prior to this, he led the Department of Electrical and Electronic Engineering, University of Kerbala, from 2013 to 2016. He holds a key scientific role in the *Renewable Energy and Power Quality Journal* (RE&PQJ).

MOHD AMRAN BIN MOHD RADZI (Senior Member, IEEE) was born in Kuala Lumpur, Malaysia, in 1978. He received the B.Eng. (Hons.) and M.Sc. degrees in electrical power engineering from Universiti Putra Malaysia (UPM), Seri Kembangan, Selangor, Malaysia, in 2000 and 2002, respectively, and the Ph.D. degree in power electronics from the University of Malaya, Malaysia, in 2010. He is currently a Professor with the Department of Electrical and Electronic Engineering, Faculty of Engineering, UPM. He is also attached with the Advanced Lightning, Power, and Energy Research (ALPER) Centre, UPM. His research and teaching interests are power electronics, power quality, and renewable energy. He is a member of the Institution of Engineering and Technology (IET), U.K.; and a Chartered Engineer.

AZURA BINTI CHE SOH (Senior Member, IEEE) received the B.Eng. degree in electronics/computer engineering and the M.Sc. degree in electrical and electronic engineering from Universiti Putra Malaysia, (UPM), Seri Kembangan, Selangor, in 1999 and 2002, respectively, and the Ph.D. degree in electrical engineering from Universiti Teknologi Malaysia, in 2011. She is an Associate Professor with the Department of Electrical and Electronic Engineering, Faculty of Engineering, UPM. She was the main Researcher of the Control System and Signal Processing (CSSP) Research Center, Department of Electrical and Electronics Engineering, UPM. She was a Coordinator of the Control and Automation of Laboratory and an Associate Researcher with the MYAGEING Institute. She is supervising three Ph.D. and six M.Sc. directly under her supervision, including ten Ph.D. and 16 M.Sc. co-supervision postgraduate students. She has published 64 journals and 69 proceedings. Her research interests include intelligent control systems, control systems, and system modeling.

HUSSEIN MOHAMMED RIDHA received the B.S. degree from the Department of Computer Engineering, University of Al-Mustansiriyah, in 2012, and the M.S.E. degree in electrical power engineering from Universiti Putra Malaysia (UPM), Seri Kembangan, Selangor, Malaysia, in 2020, where he is currently pursuing the Ph.D. degree. He has several ISI-published papers. His research interests include renewable energy, modeling of the PV cells, optimization of the PV systems, machine learning, deep machine learning, multi-objective optimization methods, and multi-criteria decision-making.

ANAS R. ALSOUD received the B.Sc. degree in computer information systems from the University of Jordan, in 2006, the M.Sc. degree in managing information technology from Salford University, U.K., in 2007, and the Ph.D. degree in informatics from the University of Reading, U.K., in 2012. He is a Professor of informatics (electronic business and commerce). Since joining AL-Ahliyya Amman University, in 2012, he has been involved with studies related to e-business, e-government, and cloud computing in developing countries. He was the Head of E-Business and M.I.S. Departments and the Dean of Student Affairs. He is currently the Vice President of International Relations and Quality; and the Director of the Center of Innovation and Excellence and the Global Engagement Centre, AL-Ahliyya Amman University. He is an expert in international accreditation and rankings for universities. He is an international advisory board member with ASIC and works on Q.S. rating and ranking systems and THE ranking systems.

VEERAPANDIYAN VEERASAMY (Member, IEEE) received the Ph.D. degree in power systems from Universiti Putra Malaysia, Malaysia, in 2021. Currently, he is a Postdoctoral Research Fellow with Nanyang Technological University, Singapore, whose research area includes power system control and optimization.

ANDREW XAVIER RAJ IRUDAYARAJ (Graduate Student Member, IEEE) received the Ph.D. degree in power systems from Universiti Putra Malaysia, Malaysia, in 2021. Currently, he is a Postdoctoral Research Fellow with Monash University, Malaysia, whose research area includes power system control and optimization.

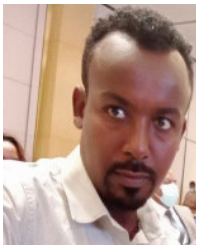

BIZUWORK DEREBEW ALEMU is currently an Assistant Professor with the Department of Statistics, Mizan-Tepi University, Ethiopia. He has published research articles in reputed journals, such as Elsevier, Springer, IET, and Taylor & Francis; and various national/international conferences. His main thirst research areas include statistical methods survival analysis, time series, structural equation modeling, categorical data analysis, and optimization algorithms. He is serving as a reviewer for various reputed journals.